Regulated Phase Separation in Nanopatterned Protein-Polysaccharide Thin Films by Spin Coating

Russell A. Banta[a,b,c], Timothy W. Collins[a,b,c], Ricky Curley[a,b,c], John O'Connell[a,b,c], Paul W. Young[b, d], Justin D. Holmes[a,b,c] and Eoin J. Flynn[a,b,c*]

[a]School of Chemistry, University College Cork, Cork, Ireland.

[b]Environmental Research Institute, Lee Road, University College Cork, Cork, Ireland.

[c]AMBER@CRANN, Trinity College Dublin, Dublin 2, Ireland.

[d]School of Biochemistry and Cell Biology, University College Cork, Ireland.

*To whom correspondence should be addressed: Tel: +35-321-490-1961; E-mail: eoin.flynn@ucc.ie

Keywords: protein, polysaccharide, biopolymer, patterning, morphology, phase separation, Ostwald ripening.

Abstract

Patterned films are essential to the commonplace technologies of modern life. However, they come at high cost to the planet, being produced from non-renewable, petrochemical-derived polymers and utilising substrates that require harsh, top-down etching techniques. Biopolymers offer a cheap, sustainable and viable alternative easily integrated into existing production techniques. We describe a simple method for the production of patterned biopolymer surfaces and the assignment of each biopolymer domain, which allows for selective

metal incorporation used in many patterning applications. Protein and polysaccharide domains were identified by selective etching and metal incorporation; a first for biopolymer blends. Morphologies akin to those observed with synthetic polymer blends and block-copolymers were realised across a large range of feature diameter (200 nm to - 20 μm) and types (salami structure, continuous, porous and droplet-matrix). The morphologies of the films were tuneable with simple recipe changes, highlighting that these biopolymer blends are a feasible alternative to traditional polymers when patterning surfaces. The protein to polysaccharide ratio, viscosity, casting method and spin speed were found to influence the final film morphology. High protein concentrations generally resulted in porous structures whereas higher polysaccharide concentrations resulted in spherical discontinuous domains. Low spin speed conditions resulted in growth of protuberances ranging from 200 nm to 22 μm in diameter, while higher spin speeds resulted in more monodisperse features, with smaller maximal diameter structures ranging from 300 nm to 12.5 μm.

Introduction

There is an urgent and growing need for micro- and nano-structured surfaces that can be produced at low environmental and economic cost. Micro- and nano-structured surfaces are essential to an array of advanced and emerging technologies. In 2016 the OECD identified 40 key emerging technologies for the future, including the “internet of things” smart devices, light technologies, regenerative medicine and tissue engineering, nanomaterials, nanodevices, carbon nanotubes, functional materials, synthetic biology, and marine and tidal power technologies. One fifth of these require patterned thin-films as integral components or as essential aspects of their production processes [1].

Micro- and nano-structured surfaces occur throughout the natural world and exhibit a range of useful properties; self-cleaning and hydrophobicity (lotus leaf)[2]; anti-reflectivity (moth eyes)[3]; iridescence (butterfly wings)[3]; anti-ice formation (kale) [4]; and anti-fouling (shark skin)[5], to name only a few. Current human manufacturing of equivalent surfaces uses top-down and bottom-up approaches: top-down is expensive, wasteful, not readily scalable, and generally restricted to planar surfaces.[3] Bottom-up requires the use of block co-polymers (BCPs) which can be expensive, are synthetically derived, require environmentally damaging organic solvents and require intricate control of the polymer-surface interface via brush layers.[6] Feature diameter and spacing is limited to sub-100 nm due to the kinetic penalties imposed on high molecular weight BCPs requiring long annealing times, limiting their applications in the optics industry. Additionally, refining BCPs of a high molecular weight to obtain a polydispersity index (PDI) close to 1 is difficult and costly.[3]

In contrast, to BCPs and other synthetic polymers, proteins innately have a PDI of 1, are cheap, abundant, renewable, do not require the use of toxic solvents and are easy to manufacture.[7] More generally, biopolymers (proteins and polysaccharides) are well-defined with varied functionality[8], hydrophilic, photostable, nontoxic, biocompatible[9], [10] and have predictable viscosities.[11] The domain sizes of features in polymer blends (synthetic and biopolymer) have been shown to exceed to 10 μm, although feature size showed considerable variance.[12]–[19] For decades biopolymer blends have been utilised in food texturing[15], [16], [19], [20], with few notable examples using biopolymer blends beyond this.[21], [22], [31], [32], [23]–[30] These, however, incorporated synthetic polymer additives, biopolymer derivatives, and/or specialist enzymes for etching or functionalisation of patterned surfaces. This renders these techniques either unsuitable for large scale manufacturing or environmentally damaging. Protein blends are expected to become prevalent in electronic, optical, chemical, mechanical, biomedical and nanotech applications in the coming years.[33]

However, the use of biopolymer blend thin films in materials science for surface patterning is further limited by the relative infancy of the field.[31]

The aim of this study was the further development of bovine serum albumin (BSA) and chitosan (Ch) blend thin films, using a protic solvent (formic acid, FA) to promote segregative phase separation in a rapid and facile manner. Current efforts to replace BCPs involve the use of synthetic polymer blends to generate patterns. However, as with BCPs, these are not renewable. To offer an alternative, renewable solution to both BCPs and synthetic polymer blends, biopolymer blend thin films must show that they can achieve similar patterns, using established methods. To this end, BSA and Ch were chosen as our biopolymers. BSA and Ch may be blended without fear of gelation when subjected to shear forces.[34] Ch is also antimicrobial[35], biocompatible and biodegradable, increasing the number of possible applications.[36] Finally, both BSA[37] and Ch[38], [39] can selectively bind metals, similar to BCPs. Synthetic polymer blends utilize selective removal of one polymer domain, followed by deposition of a metal to generate a patterned hard mask. In our work, we successfully removed the protein domain using a buffer solution, and selectively incorporated metal into the polysaccharide domain. BSA-Ch blends achieve feature diameters comparable with synthetic polymer blends.[3], [40], [41] This method could be easily employed in other studies of biopolymer blends. Furthermore, this is the first time a hard mask has been produced with bottom-up biopolymer blends. Lastly, we have successfully differentiated the growth mechanisms occurring with dissimilar blend compositions.

Experimental

Biopolymers, Casting Solutions and Substrate

Low molecular weight chitosan (Ch, 50-190 kDa, > 75 % deacetylation) and bovine serum albumin (BSA, lyophilised powder, ≥ 96 %, molecular weight ~66 kDa) were purchased from Sigma Aldrich. While the Ch we sourced was the deacetylated form of chitin (i.e. a chitin derivative, which may be considered a semisynthetic), Ch may also be sourced from fungal biomass without the need for derivatization.[42] Ch is renewable, and it is much more easily solubilized than chitin. Hence it was chosen for this work. Low molecular weight chitosan was chosen as it was shown previously shown to be easily solubilized in the FA, while not being excessively viscous.[34] Substrates used in all cases were Fisherbrand™ Microscopic Slides with Ground Edges (plain) or planar substrates. Highly polished single-crystal silicon <100> wafers (p-type, boron) with a native oxide layer of ~2 nm were also used. For FTIR, XPS, water contact angle, and selective metal inclusion, samples were deposited on a Si substrate. This was done to prevent any deformation of a glass substrate during annealing. The solvent used was formic acid (FA), 98+ %, pure (ACROS Organics™) and was diluted to 90 % w/v with distilled water before use. Casting solutions were prepared using 90 % formic acid as the solvent to ensure that the biopolymers were below their isoelectric point in solution and so, positively charged.

Solution Preparation

Biopolymers blend preparation may be found in our previous work, or in our Supporting Information. In short, stock solutions were made by dissolving biopolymers in 90 % FA, and stored at -20 ºC. Before coating, stock solutions mixed with one another and diluted with fresh FA.[34] 5 solutions were prepared. 4 w/v% BSA 1 w/v% Ch (4:1 blend ratio), 2 w/v% BSA

1 w/v% Ch (2:1 blend ratio), 1 w/v% BSA 1 w/v% Ch (1:1 blend ratio), 1 w/v% BSA 2 w/v% Ch (1:2 blend ratio) and 1 w/v% BSA 4 w/v% Ch (1:4 blend ratio).

Coating Preparation

Thin-film Casting

Thin-films were prepared using a spin coater (Speciality Coating Systems, 6800 Spin Coater Series) to produce biopolymer solution coatings of uniform thickness. Standard conditions: 30 s spin time (ramp time 5 s, dwell 25 s). Substrates were glass slides onto which single biopolymer solutions were cast. Temperature and humidity was maintained at approx. 18 ºC and 65 % relative humidity. Monitoring of humidity and ambient temperature was done by *HOBO MX Temp/RH Logger* sensor.

Atomic Force Microscopy (AFM)

Sample morphology was analysed by atomic force microscopy (AFM) using a Park Systems, XE-100 instrument under ambient conditions in non-contact mode, and this methodology was used in our previous work.[34] Scans were performed in non-contact mode with high resolution, silicon micro-cantilever tips. Topographic images were recorded at a resonance frequency of 270-300 kHz. Images were analysed using *Park XEI* and *Gwyddion*, and resulting data analysed using *Origin*. Images were flattened by removal of the background plane (using a first or second regression order). Features were then identified using the Gwyddion watershed algorithm for analysis, and descriptive statistics calculated using "Microcal Origin" software. Surface roughness (nm) and surface area ratios (%) were measured using "XEI" software. RMS (*root means square arithmetical mean roughness* or *root means square average roughness*) is the average between the height deviations and the mean line/surface, taken over the evaluation length/area. Surface area ratios (%) were

calculated by the following formula: Surface Area Ratio (%) = 100 (%) × (Geometric Area – Surface Area) / (Geometric Area). Surface feature diameters were measured using the Gwyddion watershed algorithm for scanning probe microscopy (approx. 1000 features). Film thickness was determined by AFM. AFM height scans were performed on areas which had been scratched to expose the underlying substrate.[26]

X-Ray photoelectron spectroscopy (XPS)

XPS spectra were acquired on an Oxford Applied Research Escabase XPS system equipped with a CLASS VM 100 mm mean radius hemispherical electron energy analyser with a five-channel detector arrangement in an analysis chamber with a base pressure of 10×10^{-10} mbar. Survey scans were acquired between 0-1000 eV with a step size of 0.7 eV, a dwell time of 0.5 s and pass energy of 50 eV. Core level scans were acquired at the applicable binding energy range for each core level, with a step size of 0.1 eV, dwell time of 0.1 s and pass energy of 20 eV averaged over 20 scans. A non-monochromated Al-kα x-ray source at 200 W power was used for all scans. Multiplier voltage was maintained at 2.0 kV for all acquisitions. All spectra were acquired at a take-off angle of 90º with respect to the analyser axis and were charge corrected with respect to the C 1s photoelectric line by rigidly shifting the binding energy scale to 285 eV. Data were processed using CasaXPS software where a Shirley background correction was applied and peaks were fitted to Voigt profiles.

Attenuated Total Reflection Fourier Transform Infra-Red (ATR-FTIR) Spectroscopy

Infrared spectra were recorded on a PerkinElmer Spectrum 2 FT-IR Spectrometer. Perkin-Elmer Spectrum v5.0.1 software was used to perform baseline corrections and evaluate spectra. Each spectrum was scanned between 400 and 4000 cm^{-1} with a resolution of 4 cm^{-1} and a minimum of 64 scans were collected and averaged in order to gain good quality spectra.

Selective Etching

A wet etch was used in order to selectively remove BSA over Ch due to its limited solubility. [43] Biopolymer blend films were crosslinked with a 20 wt% glutaraldehyde solution for 20 hr. Coated substrates were immersed in a buffered solution stirring for 20 hr at 300 rpm. Buffered solutions contained 200 mM Tris-HCl, pH 8.8. The substrate was then washed thoroughly with deionised water to remove residual salt. Finally, the substrate was washed with isopropanol alcohol and dried under nitrogen for analysis.

Selective metal inclusion

To confirm the results of the selective etching of BSA using a basic buffer solution, and identify the Ch domain, selective inclusion of the metal into the Ch domain used. As a 1:1 BSA-Ch blend used to identify the BSA domain using a selective etch, the 1:1 BSA-Ch blend was also used for selective metal inclusion. 1:1 blend films were prepared as described in the Thin-film Casting section, producing a film with discontinuous spheres in a matrix. After casting, films were crosslinked with a 20 wt% glutaraldehyde solution for 20 hr to prevent oversaturation of metals in the Ch domain. 1 wt% $FeCl_3$ solutions were produced with anhydrous ethanol. Biopolymer blend films were covered with 1 ml of metal solution for 15 s before spin coating. The films were then immediately spin coated for 30 s (3000 rpm, ramp time 5 s, dwell 25 s). The samples were then oxidised in a furnace at 550 ºC for 2 hr. Calcination at 800 ºC for 20 hr was used to remove the biopolymer template and any residual organic residue. No other processing steps were needed.

Water Contact Angle

Water contact angle measurements were obtained using the Ossila Contact Angle Goniometer (error ± 1º) and accompanying software Ossila Contact Angle v1.0. A deionised water droplet (5 μL) was delivered to the coated surface by a calibrated variable pipettor. Contact angles were measured in triplicate as a function of time. Measurements were taken at 10 s intervals over 160 s including measurements at 0 and 160 s.

Results and Discussion

Single Polymer Solution Thin-Films

AFM images (see **Figure S1** in Supporting Information) showed that thin-films cast from the two individual biopolymers (Ch and BSA) did not produce any phase separated patterns. Neat BSA films were totally featureless (**Figure S1**), while Ch showed partially aggregated structures, likely due to its limited solubility. Glass slides were smooth and featureless. This shows that features present in subsequent composite biopolymer films are due solely to the composite formation mechanisms and not due to structures from an individual biopolymer. This is consistent with our previous findings.[34]

BSA-Ch Thin-Films

Thin-films from Phase Separation of BSA-Ch-FA Solutions

Phase separation in polymer blend systems is the development of two distinct regions (phases) of polymers from an initially homogenous solution. Similar to oil and water, polymers which are incompatible separate from one another. Dissolving biopolymers in an acid protonates the polymer chains, promoting segregative phase separation.[15] Upon separation, topographical features develop as the film dries as the system attempts to minimize surface energy. Typically,

spheres or pores are formed as they have the lowest surface area to volume ratio. These features grow as the system continues to minimize total surface energy. [44], [45]

Figure 1 shows AFM images of BSA-Ch blend films. High resolution images each blend are provided in **Figure S2 – S6,** with accompanying line profiles provided in **Figure S7 – S11** in Supporting Information). Pores formation in the 4:1 and 2:1 BSA-Ch blend formed through different mechanisms. Pores are discussed in the supplementary information.

In the 4:1 BSA-Ch blend, increased spin speed inhibited protuberance (spherical bumps) growth, resulting in smaller, more homogeneously dispersed spheres. Feature diameter and density data (represented as mean±standard deviation, **Figure 2** and **Figure S12**) shows increased spin speed decreased protuberance diameter, and increased protuberance number per area (protuberances/μm^2). This follows the general trend observed for all films. Mean protuberance diameter decreased from 2.91 μm (500 rpm) to 0.81 μm (4000 rpm) (**Figure 1**, A1 – A5). The 4:1 BSA-Ch blend was the only blend to contain salami structures ≥ 50 μm (**Figure S13** in Supporting Information). Deposition at 500 rpm of the 4:1 blend resulted in dewetting, attributed to the feature length approaching film thickness.[17] This is known to occur during the latter stages of, and interfere with, phase separation. Low spin speeds when casting films allows more time for phase separation to occur, causing feature diameter to exceed film thickness (**Figure S12, Figure S14** in Supporting Information), leading to the salami structure. The discontinuous salami domain is composed entirely of protuberances. Pores are localised outside perimeter of the salami domains. The formation of the salami morphology at this blend ratio may explain the variation in growth mechanism compared to a high polysaccharide content blend (see below). This indicates that pores within the BSA domain (and protuberances contained within the discontinuous Ch domain) are controlled by a secondary phase separation process, which is consistent with our observations of film thickness [17], [46]. Lastly, in the 4:1 blend, higher spin coating speeds resulted in thinner samples, as

240 did blend solutions with lower viscosity (lower w/v% solutions, **Figure S14** in Supporting
241 Information for further details).

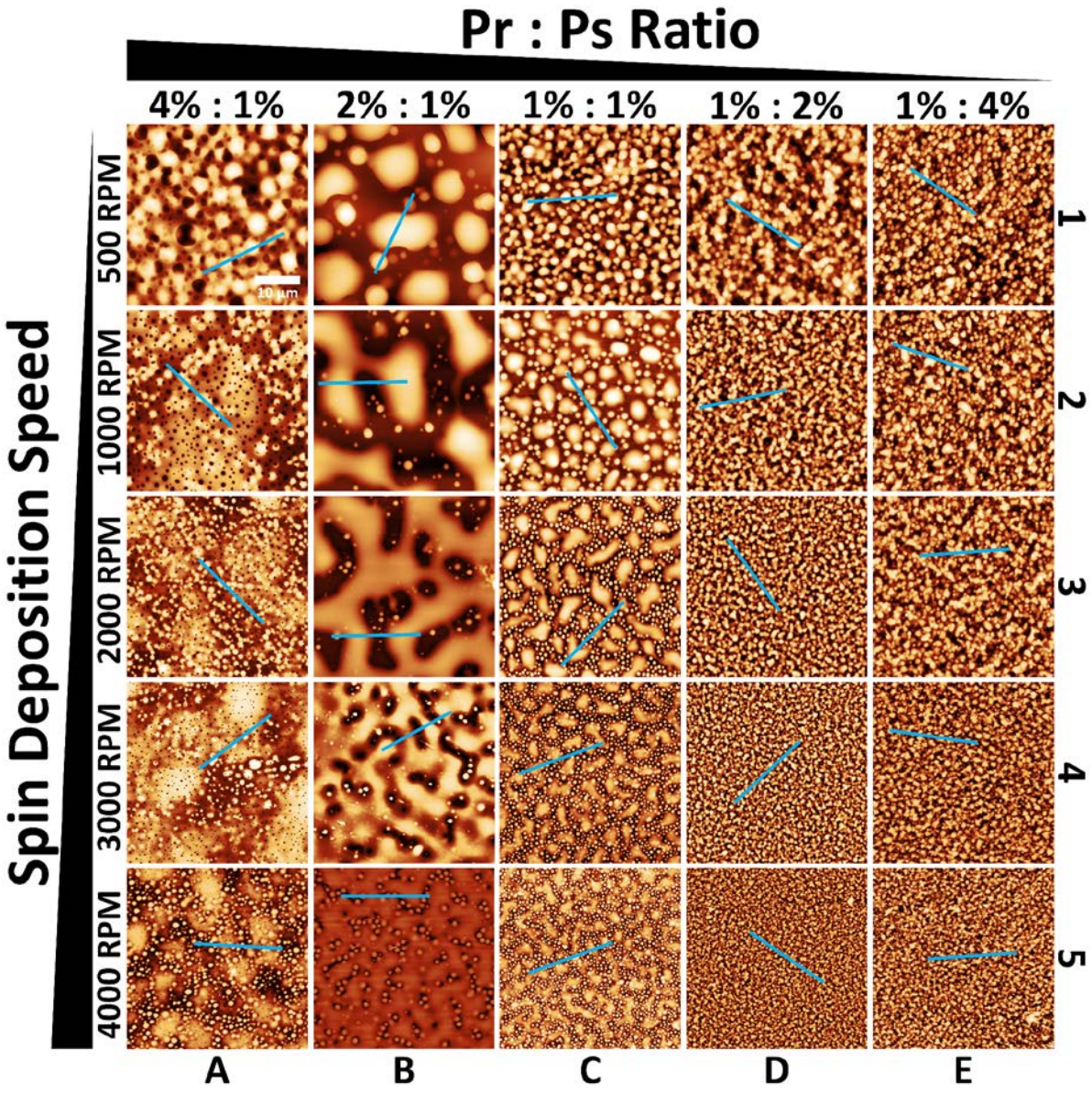

242

243 ***Figure 1:*** *AFM image grid showing results of casting thin-films at 65 % relative humidity from*
244 *specific Pr-Ps (protein-polysaccharide) solutions of BSA-Ch-FA at various spin speeds. Each*
245 *image is 40 µm × 40 µm area (scale bar 10 µm, shown in 4:1 blend at 500 rpm). In the image,*
246 *bright areas are higher and dark areas are lower. Line profile (blue lines) may be found in*
247 *each image and its corresponding* ***Figure S2 – S6*** *in Supporting Information. Column A = 4*
248 *w/v% BSA and 1 w/v% Ch (4:1), column B = 2 w/v% BSA and 1 w/v% Ch (2:1), column C =*

1 w/v% BSA and 1 w/v% Ch (1:1), column D = 1 w/v% BSA and 2 w/v% Ch (1:2), column E = 1 w/v% BSA and 4 w/v% Ch (1:4). Row 1 = 500 rpm, row 2 = 1000 rpm, row 3 = 2000 rpm, row 4 = 3000 rpm and row 5 = 4000 rpm.

At all spin speeds, protuberances follow a general trend of decreasing mean diameter with increasing spin speed (**Figure 2a**). As a result, BSA-Ch blend film root-mean-squared (RMS) roughness of the films and surface area ratio (%) decreases with increasing spin speed, discussed in more detail the Supporting Information (**Figure S15**). As protuberances are the desired morphology, a simple, predictable and efficient method of controlling feature diameter like this is highly advantageous.

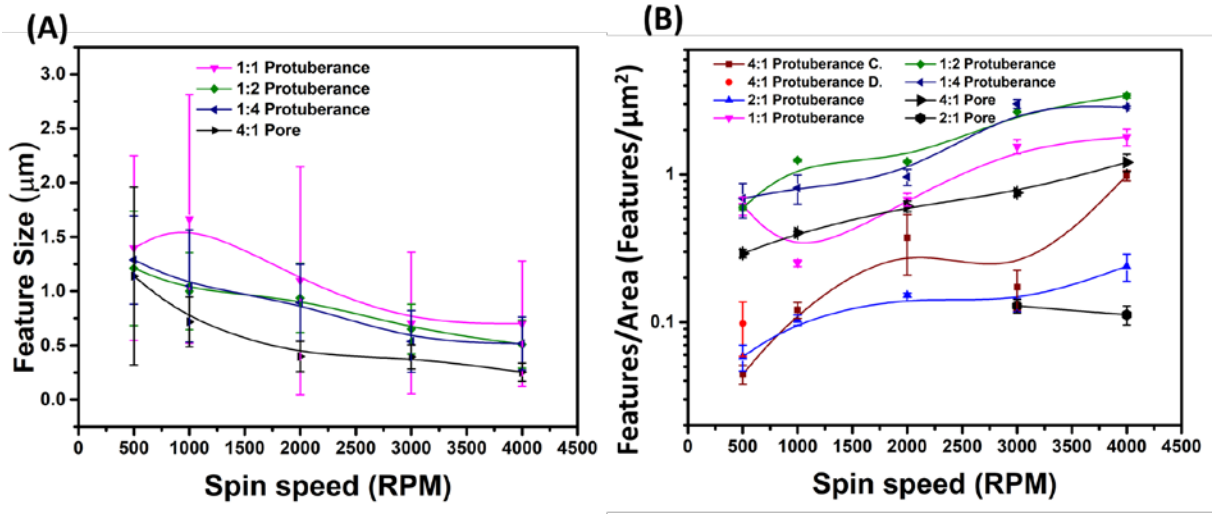

Figure 2: *Statistical analysis of BSA-Ch blends for feature diameter and feature number/area. All but the 4:1 blend refers to protuberance measurements, with the 4:1 and 2:1 blend data displaying both protuberance and pore data separately. The circular legend for the 4:1 blend refers to feature diameter in the discontinuous domain, i.e. salami structure regions.* ***A)*** *Refers to feature diameter plotted against spin speed while* ***B)*** *details features/µm^2 vs spin speed for 4:1, 2:1, 1:1, 1:2 and 1:4 blends respectively.*

Figure 1 Column B contains the most visually distinct film structures, with the largest protuberances of any blend formed. **Figure 1**, B1 and B2, show that increasing the film casting spin speed of 2:1 BSA-Ch blends reduced mean protuberance diameters from 2.91 µm (500 rpm) to 1.60 µm (1000 rpm). The same increase in rpm also narrowed protuberance size distribution (SD), from 1.5 µm – 6.1 µm to 0.7 µm – 3.2 µm. Spin speeds above 2000 rpm produced a mixed porous/protuberant (**Figure 1**, B3 – B5). Protuberance diameter decreases from 1000 rpm to 3000 rpm (1.6 µm to 0.81 µm). This reduction in protuberance diameter is less than the initial reduction from 500 to 1000 rpm (**Figure 1**, B2 – B4). Protuberance mean diameter increases at 4000 rpm (**Figure 1**, B5) to 0.99 µm. The increase in mean diameter is likely due to shear at high speeds, as increased speeds should remove solvent quicker, inhibiting growth. Spin speed thereby reduces the diameter of protuberances through faster solvent evaporation and create larger ovoid protuberances (non-spherical protuberances elongated on one axis) through shear forces, similar to the pore effect described in the 2:1 blend [18]. The number of protuberances per area increased linearly from 500 rpm to 4000 rpm with increased spin speed (**Figure 2b**). The submicron features in **Figure 1** are smaller than most biopolymer blends in the literature (typically 10 µm in diameter and above). We attribute our smaller features to the chosen biopolymers, spin speed, and chosen solvent.[12]

Solvents likely play a large role in forming the large features typically associated with biopolymer thin-films morphologies and other structures produced from biopolymer blends. Slowly evaporating blends produce large scale features.[23],[47] Low vapour pressure (non-volatile) solvents evaporate slowly, while high vapour pressure (volatile) solvents evaporate quickly producing smaller feature sizes.[47],[48] This may explain why biopolymer blends produce large features, as water is the typical solvent. [12], [49]–[51] De Jong & van de Velde segregatively phase separated whey protein/polysaccharide blends using water. Features were 5 – 10 µm in size.[12] PS/PEG blends use toluene, which is much more volatile than water,

producing features 200 – 400 nm in diameter.[40] Furthermore, using toluene as a solvent (less volatile) produces larger features than chloroform (more volatile).[47]

When the quantities of protein and polysaccharide are approximately equal (1 w/v% BSA to 1 w/v% Ch (**Figure 1**, Column C)) an intermediate state is seen, where larger, coalesced features are observed, but a continuous phase is not sufficiently formed. Protuberance diameter initially increases from approx. 1.40 µm to 1.67 µm with spin speed increase from 500 to 1000 rpm (**Figure 2a)**. This is in conjunction with a sharp decrease in protuberances per area (**Figure 2b**) suggesting a growth process. From 1000 rpm to 4000 rpm (**Figure 1**, C2 – C5), protuberance diameter decreases from 1.67 µm to 0.71 µm, while the number per area increases (**Figure 2b**). This data shows that reducing the time for solvent loss produces smaller protuberances and that there is a large degree of control over pattern formation. However, above 1000 rpm protuberances are more irregular and less circular in shape. While the 1:1 BSA-Ch blend produces smaller protuberances than previously discussed blends, higher speeds introduce an undesired pattern inhomogeneity. Increasing spin-coating speed from 2000 rpm to 4000 rpm results in increased average diameter of these irregular protuberances (2.6 – 6.0 µm). These features appear similar to high spin speed 2:1 blends (**Figure 1**, B2 – B5). The 1:1 blend at 2000 rpm (**Figure 1**, C3) adopts a morphology similar to 2:1 blend at 1000 rpm (**Figure 1**, B2) with larger protuberances interconnecting to form irregularly shaped ovoids. 3000 rpm (**Figure 1**, C4) produces flatter, larger, more branched features, similar to 2:1 BSA-Ch blends at 2000 rpm (**Figure 1**, B3). This effect is further exaggerated at 4000 rpm (**Figure 1**, C5). We attribute this to higher shear stresses on larger structures at higher spin speeds.

Reduction of the BSA ratio from 2:1 to 1:1 (**Figure 1** Column C, **Figure S4**) results in insufficient protein quantity to form a continuous phase as in **Figure 1** B3, *i.e.* phase inversion

315 does not occur preventing the pseudo pores seen in the 2:1 blend. This indicates that high
316 protein concentration is required for pore formation. The reduction of protein content to 1
317 w/v% produced a more monodisperse sample, and provided smaller feature diameters than 2:1
318 and 4:1 BSA-Ch blends, both desirable traits for patterning surfaces. Equally, the reduced BSA
319 content produced smaller protuberances, as did higher spin speeds. Complicating things
320 further, spin speeds above a certain maximum elongate the larger structures on the surface; that
321 maximum is blend dependant. The reduction of BSA w/v% (in contrast to the 2:1 and 4:1
322 blends) produces smaller BSA domains as less material is present to form these domains.
323 While mean diameter reduces with increased spin speed, larger domains increase in diameters
324 under shear with increased spin speed. Never-the-less, the 1:1 BSA-Ch blend results
325 demonstrate the ability to easily control feature diameters and features/area. This is vital for
326 maximising applicability. Use of patterned biopolymer films in a broad range of applications
327 necessitates the ability to produce an equally broad range of features diameters and
328 frequencies.[33]
329
330 1:2 (**Figure 1**, Column D and **Figure S5**) and 1:4 blends (**Figure 1**, Column E and **Figure S6**)
331 follow the simplest, and near identical, trends. Protuberance diameter decreases linearly while
332 increasing spin speed for both blends, with diameters generally smaller for the 1:2 BSA-Ch
333 blend. Mean protuberance diameter ranges from 1.21 - 0.51 µm for 1:2 blends compared to
334 1.29 - 0.52 µm for 1:4 blends, with spin speeds increased from 500 to 4000 rpm. Both the 1:2
335 and 1:4 blends show feature diameters smaller than 1:1, 2:1 and 4:1 blends. The increased
336 concentration of the continuous phase (Ch) increases viscosity, limiting coalescence thereby
337 reducing feature diameter.[33] The primary differences lie in the histograms for both blends,
338 with the 1:4 blends showing better defined peaks at higher spin speeds, indicating inhibited

growth.[52] Both blends exhibit little growth in protuberances per area until a large increase is observed from 2000 - 3000 rpm (**Figure 2b**). This demonstrates that biopolymer blends may be treated the same way as traditional polymer blends, meaning biopolymer blends can be processed with pre-established techniques. Further, this method of producing a patterned surface with biopolymer blends is much quicker than previously discussed techniques, and produces features of approximately 1 μm.[34] This is much smaller than other bottom-up biopolymer techniques, and is similar to blends produced with synthetic polymers [40], [53]–[57].

Chemical characterisation of BSA-Ch blend films

Immersing coated substrates in a basic aqueous solution selectively dissolves the readily water-soluble BSA. This allows for selective removal of the protein. **Figure 3a** shows a neat the 1:1 BSA-Ch blend, while **Figure 3b** shows both the large and small BSA domains removed from the Ch matrix. Line profile analysis shows that larger domains do not penetrate directly to the substrate, but are suspended in the Ch matrix. Smaller spherical domains protrude much deeper into the Ch domain confirming late stage dewetting. Many of the pores in **Figure 3b** contain extruded rims extending from the surface, producing a crater shape. This provides insight into the protuberances formation mechanism. Coalescence of droplets is generally broken into four steps: (i) droplet approach, (ii) matrix drainage between droplets, (iii) breakup of the matrix film and (iv) relaxation of coalesced droplet into spherical shape.[58]–[60] Drainage of the Ch matrix is observed in smaller BSA protuberances in contact with larger BSA domains. However, many pores retain this crater morphology (***Figure 3*c**). Other work on polymer blends has shown these sharp, elevated rims occur when the continuous phase climbs around the discontinuous droplets, *i.e.* pinning of the triple-phase protein-polysaccharide-air boundary,

droplet breakup, and resultant inhibited growth. [61], [62] Note that the features in our etched BSA-Ch blend are over thirty times smaller than those of polystyrene/poly(methyl methacrylate) blends, and are equivalent to polyfluorene blends. This was seen in other blends (**Figure S16** in Supporting Information) with rim height approx. 40 nm.

When using BCPs to pattern metals, metal is incorporated in to a single domain due to the different chemistries of each BCP block.[63] Ch is well known for its metal binding capacity, due to the free electron pair on the amino group.[64]–[67] $FeCl_3$ was chosen as the metal incorproate, as the amino group of Ch will chelate hard cations such as Fe^{3+}.[68] Unlike Ch, BSA binds to soft metal cations.[37] $FeCl_3$ was chosen as the metal incorporate for a second reason. Metal anions can promote, or inhibit, the binding of metal cations to proteins. In particular, the Cl^- anion has a low affinity for BSA, as it is weakly hydrated. This effect is described by the Hofmeister series.[69], [70] By choosing $FeCl_3$ as the metal precursor, both the hard nature of the metal cation, and weakly hydrated nature of the metal counter-anion, ensure that metal is incorporated only into the Ch domain. This allows for identification of the Ch phase. Water was not chosen as a solvent for $FeCl_3$, as BSA is soluble in water. Using water as a solvent for metal incorporation would result in the solubilization (and removal) of BSA during the metal incoproation step, interfering with the identification of the Ch phase. The use of anhydrous EtOH ensures the BSA domain is not solubilized. Though the number of factors considered may seem excessive, trying to incoproate metal into a singular biopolymer domain is no small feat. **Figure 3d** confirms that the continuous phase is Ch due to the Fe_3O_4 uptake mirroring the BSA-Ch blend. Large BSA ovoid protuberances are reflected as large irregularly shaped voids (large areas absent of metal uptake) in **Figure 3d**. Smaller BSA protuberances are reflected as circular pores in the metallic film. Both the BSA etch and metal incorporation do not reveal the bottom silicon substrate, indicating a thin layer of Ch separates the BSA droplets from the substrate, blocking the Si surface, a feature observed in

388 almost all polymer blends.[53] Any application this may have as a hard mask would require
389 perforation of the BSA domain to the Si substrate, as the Si must be accessible to the etchant.
390 To the best of our knowledge, purely lateral phase separation of a polymer blend has only been

achieved once.[53]

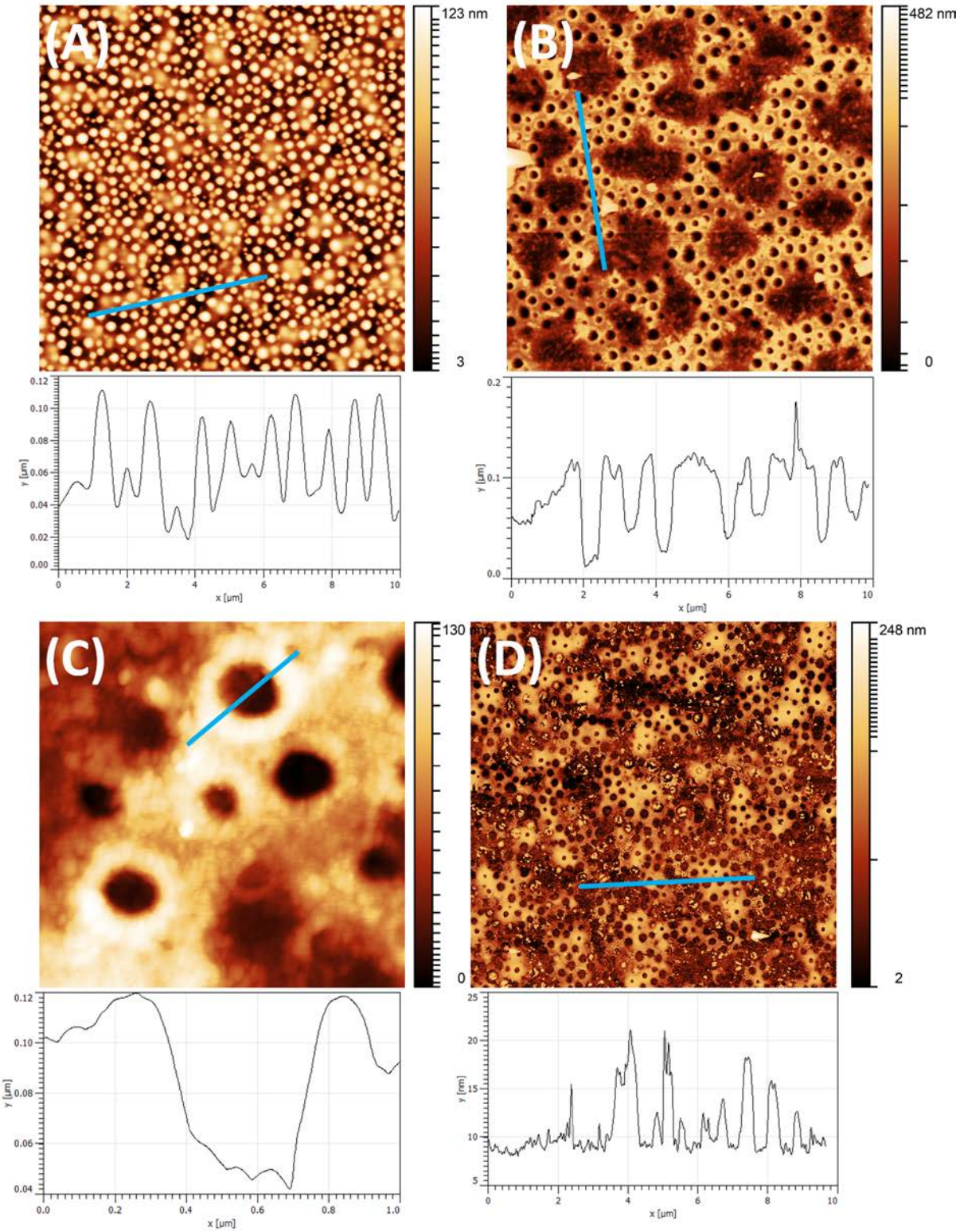

Figure 3: *AFM images and surface profiles of 1:1 BSA-Ch blends, 3000 rpm on planar silicon substrates. A) Refers to blend before Tris-HCl etch. B) Refers to blend post selective etching.*

C) Enhanced view of selectively etched BSA domains demonstrating extruded rim structure in Ch film. D) Refers to blend post selective metal incorporation and calcination.

Figure 4A shows FTIR transmission spectra of the biopolymer blend after various processes. This was done to confirm chemical changes in the sample after BSA removal, crosslinking, and calcination. For clarity of comparison, a bare Si wafer, plain BSA, and plain Ch were analysed so that their identifying peaks could be differentiated from any unique to the blend films. The bare Si wafer (**Figure 4A**, spectra i) has standard identifying peaks at 514 (Si–O deformation)[71], 611 (Si–Si bond vibrations in the bulk)[72], 739 (O–H out of plane bending)[71], 891 (Si–O–H mode due to oxidation of upper silicon layer)[72] and 1108 cm^{-1} (Si–O–Si asymmetric stretching).[73] The shape and intensity of these peaks are similar for all samples**.** The neat BSA film spectrum (**Figure 4A**, spectra ii) contained a weak band at 1376 cm^{-1} due to CH_3 symmetric bending.[74] The amide I, and amide II modes of BSA were observed at 1656 cm^{-1} and 1544 cm^{-1} respectively.[74] The amide II' transmission band is seen at 1448 cm^{-1}.[75] The peak at 3208 cm^{-1} can be assigned to asymmetric and symmetric H–O–H stretching, resulting from residual water in the film after casting.[74] Peaks in the Ch spectra (**Figure 4A**, spectra iii) are observed at 1718 cm^{-1}, 1573 cm^{-1} and 1374 cm^{-1} corresponding to the amide I, amide II, and amide III bands, respectively.[74], [76], [77] The peak at 1445 cm^{-1} can be assigned to an N-H bending of Ch. [78], [79]

The 1:1 blend (**Figure 4A**, spectra iv) exhibited no new peaks indicating no new bonds occur. The Amide II peak for the non-crosslinked BSA film and the non-crosslinked Ch film becomes less prominent after crosslinking (**Figure 4A**, spectra v and vi). This indicates a reduction in free amines after crosslinking and the formation of a Schiff base.[80] After crosslinking, the 1:1 BSA-Ch blend (**Figure 4A**, spectra vii) has a peak at 3264 cm^{-1}: this is due to water retained in the film after nitrogen drying. The crosslinked 1:1 film's amide II

peaks are less prominent post crosslinking, confirming crosslinking occurred. As the peaks appear similar to those in the neat biopolymer films after crosslinking, we can infer only intramolecular crosslinking has occurred which would suggest no BSA remains on the film after etching. This is expected as BSA is segregated from the Ch domain. However, some small degree of intermolecular crosslinking may occur at the BSA-Ch interface, though this may be below the detection limit of the machine.[10]

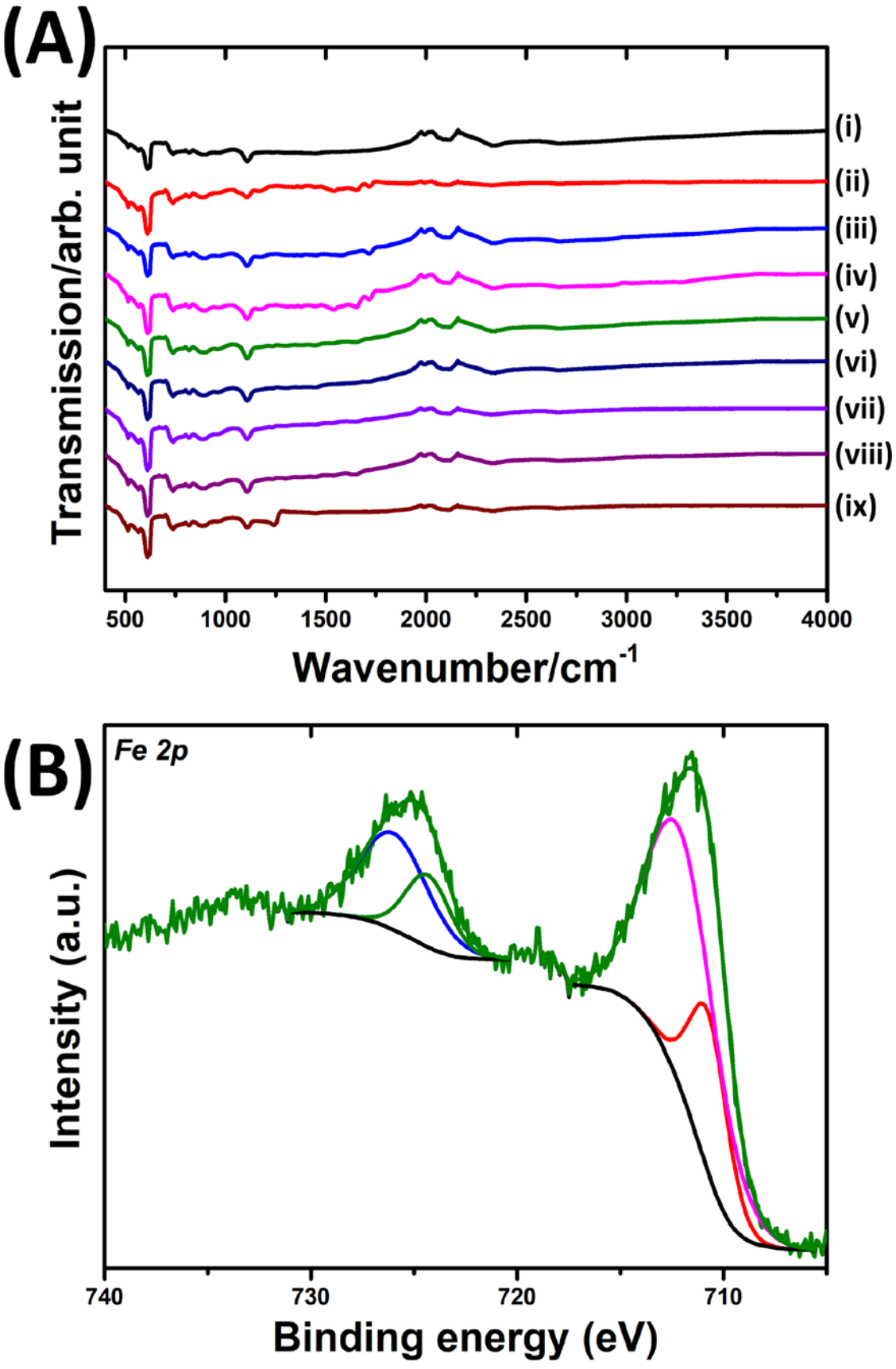
(A)
Transmission/arb. unit
(i)
(ii)
(iii)
(iv)
(v)
(vi)
(vii)
(viii)
(ix)
500
1000
1500
2000
2500
3000
3500
4000
Wavenumber/cm-1
(B)
Fe 2p
Intensity (a.u.)
740
730
720
710
Binding energy (eV)

425

Figure 4: A) *FTIR spectra of* ***i)*** *bare silicon wafer,* ***ii)*** *1 w/v% BSA film 3000 rpm deposition,* ***iii)*** *1 w/v% Ch film 3000 rpm deposition,* ***iv)*** *1:1 BSA-Ch blend film 3000 rpm deposition,* ***v)*** *1 w/v% BSA film 3000 rpm deposition crosslinked,* ***vi)*** *1 w/v% Ch film 3000 rpm deposition crosslinked,* ***vii)*** *1:1 BSA-Ch blend film 3000 rpm deposition crosslinked,* ***viii)*** *1:1 BSA-Ch blend crosslinked film after Tris-HCl etch and* ***ix)*** *porous iron oxide matrix after annealing and calcination treatment.* ***B)*** *Shows the XPS Fe 2p spectra of iron porous matrix after annealing and calcination treatment.*

The spectra of the etched film (**Figure 4A**, spectra viii) after crosslinking retains the BSA peaks. This suggests residual BSA on the surface due to intermolecular crosslinking, or after washing. Calcination of the BSA-Ch blend after metal incorporation results in a spectra with no characteristic peaks of BSA or Ch, indicating their removal (**Figure 4A**, spectra ix). The more prominent Si–O–Si band at 1108 cm^{-1} after calcination indicates a thicker oxide layer than the native oxide of the original Si wafer. This is further confirmed by the peak in the bare Si wafer (1237 cm^{-1}) shifting to 1245 cm^{-1}, which occurs when oxide thickness increases, a consequence of the long calcination time and high temperature required to ensure complete biopolymer removal.[81] This peak corresponds to the longitudinal optical phonon of SiO_2 (LO) around 1250 cm^{-1}, which occurs in thermal oxides.[82] Fe peaks were not observed at 630 cm^{-1} or 540 cm^{-1}, characteristic of magnetite and hematite respectively. FTIR confirmed successful crosslinking of the biopolymer film before etching and successful removal of the biopolymers after calcination.[83]

XPS was used to determine whether the iron present was predominantly hematite or magnetite to confirm metal incorporation and oxidation (**Figure 4B**). The chemical composition of the iron oxide matrix before/after annealing and calcination was confirmed by Fe 2p XPS studies. Following calcination, the Fe 2p core level spectrum (see **Figure 4B**)

consists of two sharp peaks at 711.6 eV (Fe $2p_{3/2}$) and at 725.7 eV (Fe $2p_{1/2}$) which are broadened due to the presence of Fe^{2+} and Fe^{3+} ions. Curve-fitting using Gaussian–Lorentzian line shapes provides individual binding energies of 710.7/724.3 eV (assigned to Fe^{2+}) and 712.0/726.0 eV (Fe^{3+}) in agreement with literature reports.[84] The Fe^{3+}/Fe^{2+} ratio was estimated to be approx. 2:1, typical of magnetite. The C1s peak is nominal demonstrating the effective removal of biopolymeric material during calcination, and is consistent with extraneous carbon species adsorbed during sample preparation (**Figure S17** in Supporting Information).

Protuberance Growth in Blend Thin-Films

Feature diameter determines the properties of a surface, such as pattern transferability, hydrophobicity, etc. SDs can be used provide insight into film features and their growth mechanisms[52]. This allows control of feature formation to optimise films for specific applications. Protuberance diameter data was extracted from AFM images and presented as SDs in normalized frequency histograms (**Figure 5**). Information about pore diameter and mechanism of pore formation can be found in the Supporting Information (**Figure S18)**. All blends exhibit multimodal SDs with protuberances of large diameter at low spin speeds. Increasing spin speed reduces the number of modes and shifts population weight to narrower diameters, further indicating a nucleation and growth process. This also indicates that faster spin speeds, up to certain thresholds, produce more homogenously distributed features of more uniform diameter. This is crucial to production of effective patterned thin films. The 2:1 BSA-Ch blend at 4000 rpm (**Figure 5b**) is an exception to the above, exhibiting a bimodal SD with peaks at 1.3 µm and 1.5 µm protuberance diameters. This is likely due to shear effects at higher spin speeds.

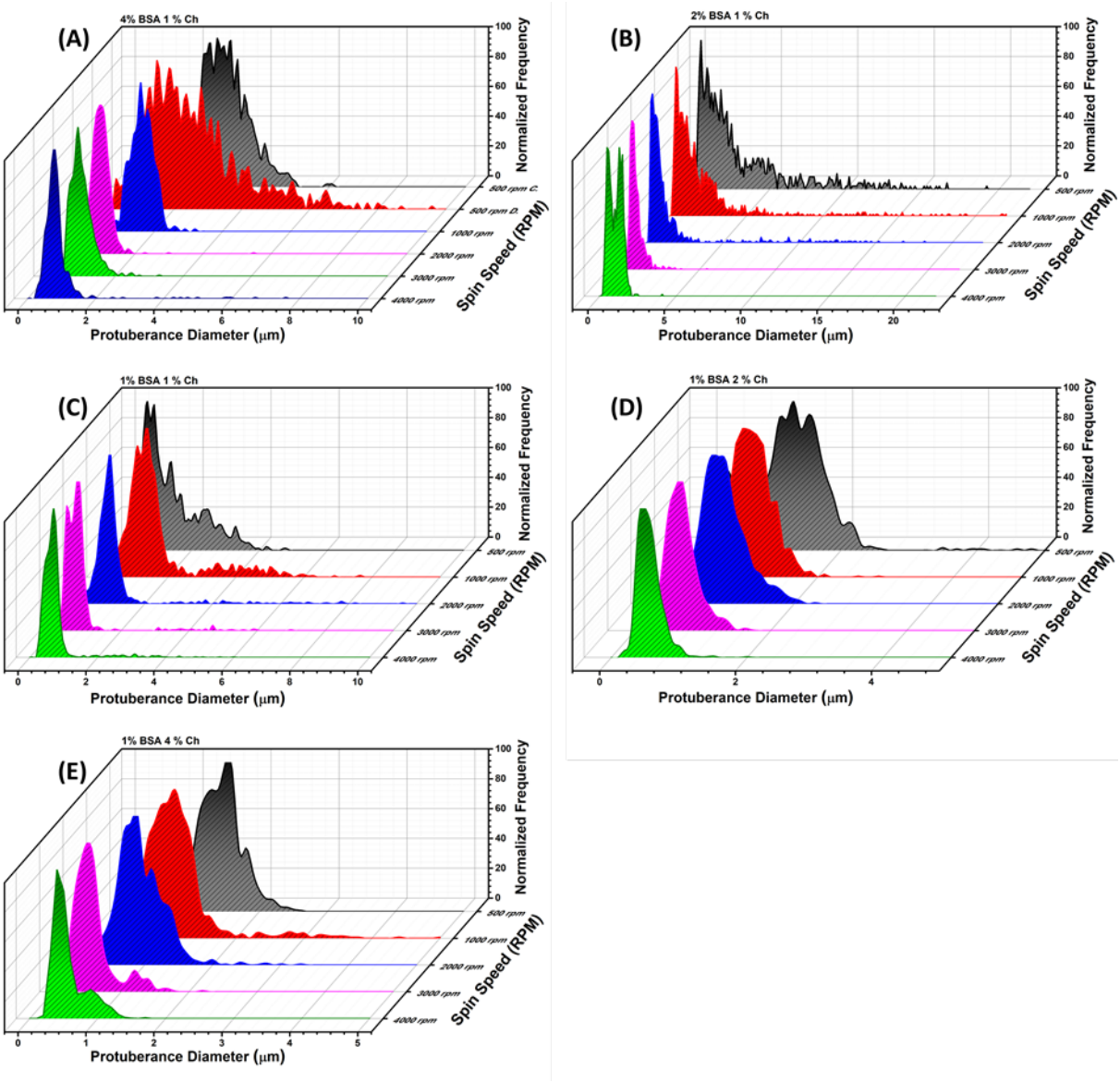

Figure 5: *Statistical analysis of BSA-Ch blends for protuberances and frequency of protuberance sizes. Each curve based on approx. 1000 protuberance diameter measurements. All but the 4:1 blend refers to protuberance measurements contained within the matrix, with the 4:1 blend data displaying protuberance data for the continuous and discontinuous (salami structure) domain.* ***A – E*** *displays feature frequency vs diameter of observed features for 4:1, 2:1, 1:1, 1:2 and 1:4 blends respectively.*

Ostwald ripening occurs by the transfer of material from smaller features to larger features by diffusion. The result is smaller features reducing in diameter while larger features increase in diameter.[52] This is distinct from coalescence, where multiple spherical features merge to form a larger version of the feature with lower surface area to volume ratio. Ostwald ripening results in broader SDs and is undesirable. SDs arising from these processes have distinct identifiable characteristics. Curve fitting may be used to determine the modality of the SD (either unimomodal or polymodal), identify the mode diameter (Mo), and centre of gravity (Xc) of the identified peaks.[85] Typically, this includes the fitting of a lognormal curve to the SD. [52], [85]–[88] Lognormal peak fitting was achieved using the non-linear least squares method.[88], [89]

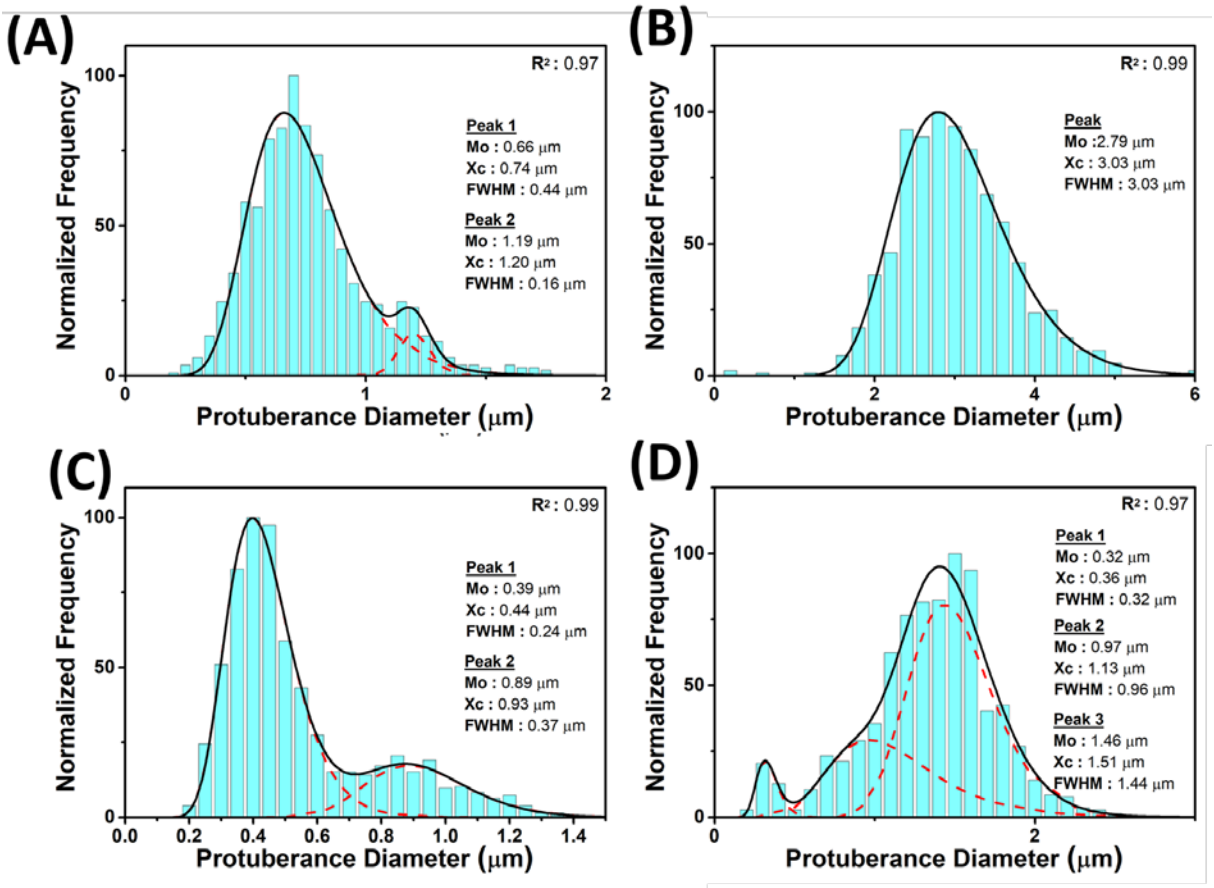

Figure 6: *Protuberance SD of* ***A)*** *4:1 BSA-Ch blend, 4000 rpm deposition,* ***B)*** *4:1 BSA-Ch blend, 500 rpm deposition,* ***C)*** *1:4 BSA-Ch blend, 4000 rpm deposition and* ***D)*** *1:4 BSA-Ch*

blend, 500 rpm deposition. The black curve (solid) denotes the best unimodal or polymodal fit with the distribution. The deconvouted peaks, shown in red (dashed), show the separate populations in the SD.

The 4:1 blend exhibits coalescence characteristics; increased feature diameter and peak broadening corresponding to longer evaporation times (**Figure 6a** and **b**). Additionally, the SD transitions from a bimodal distribution to unimodal distribution.[90] In contrast, the 1:4 BSA-Ch blend exhibits Ostwald ripening characteristics; feature diameter increases with longer evaporation time (**Figure 6c** and **d**), but formation of an extra peak (at approx. 0.3 µm) is observed with longer drying time (Peak 1, **Figure 6d**), indicating production of smaller particles, characteristic of Ostwald ripening. Increasing the concentration of Ch increased the continuous phases viscosity, resulting in Ostwald ripening being the dominant growth mechanism.[33]

These results show sub-micron features may be achieved using industrial standard deposition techniques. This technique produces rapid pattern realisation, without requiring extensive environmental controls such as temperature or humidity regulation. Feature diameter and frequency/area are substantially similar to synthetic polymer blends. This means that biopolymer blends could be incorporated into existing production processes for applications where biopolymers offer a distinct advantage, with all the environmental and economic benefits that come with using renewable resources. Furthermore, assignment of the protein and polysaccharide domain was possible due to selective etching and metal incorporation. Both techniques show promise as a method of identification of each domain (inaccessible to typical staining techniques at such a small scale). This is simply achieved by the use of a crosslinking agent, aqueous buffer and cheap metal additive, avoiding the use of expensive or specialist enzymes for identification. The attraction of these techniques is the ability to identify each

519 domain without reliance on highly sensitive surface specific methods. Furthermore, these
520 techniques compliment other facile surface probing techniques such as water contact angle
521 measurements, which show clear differences when analysing the various surfaces encountered
522 (**Figure S19**). Though incorporation and etching provides insight into the internal structure
523 (and thereby formation mechanism) of the film, they do little to inform us of the chemical state
524 of the crosslinked blend at the interface. Higher sensitivity ATR-FTIR would be required to
525 determine if crosslinking occurs at the interface. Deconvolution of the SD clearly shows the
526 presence of 2 growth mechanisms (Ostwald ripening and coalescence). Understanding of the
527 growth mechanisms is invaluable when choosing protein:polysaccharide ratios for surface
528 patterning. Selective incorporation of a metal salt could further be enhanced by use of other
529 metal salt derivatives, varying weight percentage of the salt type or varying contact time with
530 the blend film. It would be interesting to see if other salts could show preference to the protein
531 domain when incorporating into the blend film.

532

533 **Conclusion**

534 Spin speed and blend ratio are major factors when determining feature diameter, growth
535 mechanism and morphology. Blends generally showed a decrease in feature diameter and
536 roughness, while increasing in features per area with increasing spin speeds and polysaccharide
537 content. Faster drying times (high spin speeds) generally resulted in smaller features, while
538 longer drying times (low spin speeds) resulted in larger features. Simply put, faster spin speeds
539 increase the evaporation rate, limiting the amount of time features have to grow. Increasing
540 viscosity by increasing the relative Ch ratio reduced feature diameter due to lowered polymer
541 mobility. As Ch content is increased, it creates a viscous, honey-like matrix in which BSA
542 domain growth is hindered. Faster spin speeds resulted in more monodisperse blend SD's,

unless banding occurred due to shear effects at high speed. Protein:polysaccharide ratio played an important role in determining morphology. Increasing the relative BSA ratio resulted in larger BSA domains, and banding of the BSA domain at high shear due to the difference in viscosity between the two phases.[18] Selective etching and selective incorporation of the metal salts in the Ch domain allowed for protuberances to be assigned as the BSA domain, a first for biopolymer blends. Coalescence was inhibited in 1:4 BSA-Ch blends due to the increased viscosity of the blend, with feature growth described by Ostwald ripening. 4:1 blends grew by a coalesence mechanism. 1:2 and 1:4 BSA-Ch blends have the smallest circular protuberances. This is attributable to the blend solutions high viscosity and low amount of BSA to form a discontinuous phase. The 1:1 blend smaller, circular features decrease in diameter, while larger ovoid features increase in diameter at higher spin speeds (i.e. high shear). This shows inhibited growth of the film morphology at higher spin speeds, and (similar to the 2:1 blend at 1000 rpm) an attempt to phase invert its morphology. Porous films are formed in the 4:1 BSA-Ch blend. Pores decrease in diameter with increasing spin speed. Pores are produced from a solvent rich phase. The 2:1 blend phase inverts at high spin speeds. After phase inversion, pores increase in diameter with increasing spin speed due to high shear elongating their domains.

This work demonstrates that protein-polysaccharide blends can be used to rapidly produce biopolymer thin films with sub-micron patterns, all without requiring extracting, refinement and production of synthetic polymer precursors. Due to their patterns, these unique biopolymer thin-films present a vast spectrum of possible applications. These range from simple applications including traditional packaging alternatives and smart foods production, to more complex applications such as hydrophobic textile coatings, lithographic templates, antireflective coatings, and state-of-the-art hierarchal designs used in biomedicine or responsive membranes.[22], [33] Feature growth mechanisms were identified through analysis

of the SD. We did not find any previous attempts into the literature to determine the growth mechanism, which may be one reason biopolymer blends thus far have had such large feature diameters. Not only do these blends use environmentally benign and economically cheap biopolymers, but they have feature diameters on a scale with those of synthetic polymer blends, while utilizing industrially viable methods. This bottom-up method allows for instant pattern production without the need for complex equipment and techniques such as e-beam lithography. Patterns may be produced using benchtop equipment, without the long annealing times associated with synthetic polymers. Biopolymer blends are projected to play a pivotal in future manufacturing of biomedical, electronic, sensor and optical components. [22], [32], [33] Research of into the properties of biopolymer blends thin-film surface morphologies is an emerging field, and our method for producing these blends in a controlled manner is a progressive step in the adoption of these films in modern technologies.

Acknowledgements

Dr. Joseph Tobin and Richard Curly of Glantreo Ltd., Ireland, Dr. John O'Connell of the Materials Chemistry and Analysis Group, University College Cork, Cork, Ireland. The Irish Research Council for Science, Engineering and Technology is also acknowledged for financial support of the work.

Supporting Information Available:

References

[1] OECD, "Future Technology Trends," in *OECD Science, Technology, and Innovation Outlook, 2016*, 2016, pp. 77–125.

[2] A. B. López, J. C. De La Cal, and J. M. Asua, "Highly Hydrophobic Coatings from

Waterborne Latexes," *Langmuir*, vol. 32, no. 30, pp. 7459–7466, 2016.

[3] P. Mokarian-Tabari *et al.*, "Large Block Copolymer Self-Assembly for Fabrication of Subwavelength Nanostructures for Applications in Optics," *Nano Lett.*, vol. 17, no. 5, pp. 2973–2978, May 2017.

[4] E. Alizadeh-Birjandi and H. P. Kavehpour, "Plant leaves icephobicity," *J. Coatings Technol. Res.*, 2017.

[5] Y. F. Fu, C. Q. Yuan, and X. Q. Bai, "Marine drag reduction of shark skin inspired riblet surfaces," *Biosurface and Biotribology*, vol. 3, no. 1, pp. 11–24, 2017.

[6] D. Borah, S. Rasappa, R. Senthamaraikannan, J. D. Holmes, and M. A. Morris, "Tuning PDMS brush chemistry by UV-O3 exposure for PS-b-PDMS microphase separation and directed self-assembly," *Langmuir*, vol. 29, no. 28, pp. 8959–8968, 2013.

[7] J. C. Blackstock, "Carbohydrates," in *Guide to Biochemistry*, 1st ed., J. C. Blackstock, Ed. Glasgow: Butterworth-Heinemann, 1989, pp. 20–31.

[8] R. L. Whistler, "Solubility of Polysaccharides and Their Behavior in Solution," in *Carbohydrates in Solution*, 1st ed., Horace S. Isbell, Ed. Amer Chemical Society, 1973, pp. 242–255.

[9] M. C. García, "Drug delivery systems based on nonimmunogenic biopolymers," in *Engineering of Biomaterials for Drug Delivery Systems*, 1st ed., A. Parambath, Ed. Swanston, Cambridge: Woodhead Publishing, 2018, pp. 317–344.

[10] X. Ma *et al.*, "A Biocompatible and Biodegradable Protein Hydrogel with Green and Red Autofluorescence: Preparation, Characterization and In Vivo Biodegradation Tracking and Modeling," *Sci. Rep.*, vol. 6, p. 19370, May 2016.

[11] D. R. Picout and S. B. Ross-Murphy, "Rheology of Biopolymer Solutions and Gels," *Sci. World J.*, vol. 3, pp. 105–121, Mar. 2003.

[12] S. de Jong and F. van de Velde, “Charge density of polysaccharide controls microstructure and large deformation properties of mixed gels,” *Food Hydrocoll.*, vol. 21, no. 7, pp. 1172–1187, 2007.

[13] N. A. Gengec, U. Cengiz, and H. Y. Erbil, “Superhydrophobic perfluoropolymer/polystyrene blend films induced by nonsolvent,” *Appl. Surf. Sci.*, vol. 383, pp. 33–41, Oct. 2016.

[14] P. Xavier, P. Rao, and S. Bose, “Nanoparticle induced miscibility in LCST polymer blends: critically assessing the enthalpic and entropic effects,” *Phys. Chem. Chem. Phys.*, vol. 18, no. 1, pp. 47–64, Dec. 2016.

[15] F. van de Velde, E. H. A. de Hoog, A. Oosterveld, and R. H. Tromp, “Protein-Polysaccharide Interactions to Alter Texture,” *Annu. Rev. Food Sci. Technol.*, vol. 6, no. 1, pp. 371–388, Apr. 2015.

[16] M. F. Butler and M. Heppenstall-Butler, “Phase separation in gelatin/dextran and gelatin/maltodextrin mixtures,” *Food Hydrocoll.*, vol. 17, no. 6, pp. 815–830, Nov. 2003.

[17] A. Hirose, K. Shimada, C. Hayashi, H. Nakanishi, T. Norisuye, and Q. Tran-Cong-Miyata, “Polymer networks with bicontinuous gradient morphologies resulting from the competition between phase separation and photopolymerization †,” *Soft Matter*, vol. 12, no. 6, pp. 1820–1829, 2016.

[18] B. Wolf, R. Scirocco, W. J. Frith, and I. T. Norton, “Shear-induced anisotropic microstructure in phase-separated biopolymer mixtures,” *Food Hydrocoll.*, vol. 14, no. 3, pp. 217–225, May 2000.

[19] I. T. Norton and W. J. Frith, “Microstructure design in mixed biopolymer composites,” *Food Hydrocoll.*, vol. 15, no. 4–6, pp. 543–553, Jul. 2001.

[20] H. Firoozmand and D. Rousseau, “Microstructure and elastic modulus of phase-separated gelatin–starch hydrogels containing dispersed oil droplets,” *Food Hydrocoll.*, vol. 30, no. 1, pp. 333–342, Jan. 2013.

[21] I. C. Hoeger *et al.*, “Bicomponent Lignocellulose Thin Films to Study the Role of Surface Lignin in Cellulolytic Reactions,” *Biomacromolecules*, vol. 13, no. 10, pp. 3228–3240, Oct. 2012.

[22] N. Nady and S. H. Kandil, “Novel Blend for Producing Porous Chitosan-Based Films Suitable for Biomedical Applications,” *Membranes (Basel).*, vol. 8, no. 1, p. 2, Jan. 2018.

[23] K. Trommer, B. Morgenstern, F. Gähr, and F. Hermanutz, “SUB-MICROMETER STRUCTURED TEXTILE COATINGS GENERATED FROM CELLULOSE BASED POLYMER BLENDS,” *Lenzinger Berichte*, vol. 87, pp. 151–161, 2009.

[24] L. Taajamaa, O. J. Rojas, J. Laine, K. Yliniemi, and E. Kontturi, “Protein-assisted 2D assembly of gold nanoparticles on a polysaccharide surface †,” *Chem. Commun.*, vol. 49, no. 13, pp. 1318–1320, 2013.

[25] P. I. C. Claro, A. R. S. Neto, A. C. C. Bibbo, L. H. C. Mattoso, M. S. R. Bastos, and J. M. Marconcini, “Biodegradable Blends with Potential Use in Packaging: A Comparison of PLA/Chitosan and PLA/Cellulose Acetate Films,” *J. Polym. Environ.*, vol. 24, no. 4, pp. 363–371, Dec. 2016.

[26] L. Taajamaa, O. J. Rojas, J. Laine, and E. Kontturi, “Phase-specific pore growth in ultrathin bicomponent films from cellulose-based polysaccharides,” *Soft Matter*, vol. 7, no. 21, p. 10386, Oct. 2011.

[27] F. Chen, X. Monnier, M. Gällstedt, U. W. Gedde, and M. S. Hedenqvist, “Wheat gluten/chitosan blends: A new biobased material,” *Eur. Polym. J.*, vol. 60, pp. 186–197,

Nov. 2014.

[28] F. Chen, M. Gällstedt, R. T. Olsson, U. W. Gedde, and M. S. Hedenqvist, “A novel chitosan/wheat gluten biofoam fabricated by spontaneous mixing and vacuum-drying,” *RSC Adv.*, vol. 5, no. 114, pp. 94191–94200, Nov. 2015.

[29] F. Walha, K. Lamnawar, A. Maazouz, and M. Jaziri, “Rheological, Morphological and Mechanical Studies of Sustainably Sourced Polymer Blends Based on Poly(Lactic Acid) and Polyamide 11.,” *Polymers (Basel).*, vol. 8, no. 3, Feb. 2016.

[30] W. Cao, A. Wang, D. Jing, Y. Gong, N. Zhao, and X. Zhang, “Novel biodegradable films and scaffolds of chitosan blended with poly(3-hydroxybutyrate),” *J. Biomater. Sci. Polym. Ed.*, vol. 16, no. 11, pp. 1379–1394, Jan. 2005.

[31] C. Czibula *et al.*, “Design of Friction, Morphology, Wetting, and Protein Affinity by Cellulose Blend Thin Film Composition,” *Front. Chem.*, vol. 7, no. Article 239, pp. 1–10, May 2019.

[32] V. Gopishetty, Y. Roiter, I. Tokarev, and S. Minko, “Multiresponsive Biopolyelectrolyte Membrane,” *Adv. Mater.*, vol. 20, no. 23, pp. 4588–4593, Dec. 2008.

[33] X. Hu, P. Cebe, A. S. Weiss, F. Omenetto, and D. L. Kaplan, “Protein-based composite materials,” *Mater. Today*, vol. 15, no. 5, pp. 208–215, May 2012.

[34] R. A. Banta, T. W. Collins, R. A. Curley, P. W. Young, J. D. Holmes, and E. J. Flynn, “Nanopatterned protein-polysaccharide thin films by humidity regulated phase separation,” *J. Colloid Interface Sci.*, vol. 532, pp. 171–181, Dec. 2018.

[35] G. D. Jovanović, A. S. Klaus, and M. P. Nikšić, “Antimicrobial activity of chitosan coatings and films against Listeria monocytogenes on black radish,” *Rev. Argent. Microbiol.*, vol. 48, no. 2, pp. 128–136, Apr. 2016.

[36] M. do C. Teixeira, A. Santini, and E. B. Souto, “Delivery of Antimicrobials by Chitosan-

688 Composed Therapeutic Nanostructures," in *Nanostructures for Antimicrobial Therapy: Nanostructures in Therapeutic Medicine Series*, 1st ed., A. Ficai and A. M. Grumezescu, Eds. Elsevier, 2017, pp. 203–222.

691 [37] B. Saha, S. Chakraborty, and G. Das, "A Rational Approach for Controlled Adsorption of Metal Ions on Bovine Serum Albumin−Malachite Bionanocomposite," *J. Phys. Chem. C*, vol. 114, no. 21, pp. 9817–9825, Jun. 2010.

694 [38] M. Oliveira, J. A. Simoni, and C. Airoldi, "Chitosan metal-crosslinked beads applied for n-alkylmonoamines removal from aqueous solutions – a thermodynamic study," *J. Chem. Thermodyn.*, vol. 73, pp. 197–205, Jun. 2014.

697 [39] R. B. Hernández *et al.*, "Coordination study of chitosan and Fe3+," *J. Mol. Struct.*, vol. 877, no. 1–3, pp. 89–99, Apr. 2008.

699 [40] X. Guo *et al.*, "A New Strategy of Lithography Based on Phase Separation of Polymer Blends.," *Sci. Rep.*, vol. 5, no. Article 15947, Oct. 2015.

701 [41] Y. J. Donie *et al.*, "Light trapping in thin film silicon solar cells *via* phase separated disordered nanopillars," *Nanoscale*, vol. 10, no. 14, pp. 6651–6659, Apr. 2018.

703 [42] G. S. Dhillon, S. Kaur, S. K. Brar, and M. Verma, "Green synthesis approach: Extraction of chitosan from fungus mycelia," *Critical Reviews in Biotechnology*, vol. 33, no. 4. pp. 379–403, Dec-2013.

706 [43] D. J. M. And and J. J. E. Hardy, "Applications of Functionalized Chitosan in Catalysis†," *Ind. Eng. Chem. Res.*, vol. 44, no. 23, pp. 8499–8520, 2005.

708 [44] P. Van De Witte, P. J. Dijkstra, J. W. A. Van Den Berg, and J. Feijen, "Phase separation processes in polymer solutions in relation to membrane formation," *ELSEVIER J. Membr. Sci.*, vol. 117, pp. 1–31, 1996.

711 [45] L. H. Sperling, "Concentrated Solutions, Phase Separation Behavior, and Diffusion," in

Introduction to Physical Polymer Science, 4th ed., Hoboken, NJ, USA: John Wiley & Sons, Inc., 2005, pp. 145–195.

[46] M. Vonka and J. Kosek, "Modelling the morphology evolution of polymer materials undergoing phase separation," *Chem. Eng. J.*, vol. 207, pp. 895–905, 2012.

[47] M. Voigt *et al.*, "The interplay between the optical and electronic properties of light-emitting-diode applicable conjugated polymer blends and their phase-separated morphology," *Org. Electron.*, vol. 6, no. 1, pp. 35–45, Feb. 2005.

[48] O. Aschenbrenner, S. Supasitmongkol, M. Taylor, and P. Styring, "Measurement of vapour pressures of ionic liquids and other low vapour pressure solvents," *Green Chem.*, vol. 11, no. 8, p. 1217, Aug. 2009.

[49] A. N. Nesmeyanov and E. V Kikxadze, "Concentration of proteins as a result of the phase separation of water-protein-polysaccharide systems Part 1. Phase equilibria in water-milk proteins-plysaccharide systems," *Nahrung*, vol. 30, no. 6, pp. 591–599, 1986.

[50] A. N. Nesmeyanov, N. A. Zhuravskaya, E. V Kiknadze, and V. B. Tolstoguzov, "Concentration of proteins as a result of the phase separation of water-protein-polysaccharide systems Part 2. Concentration of milk proteins," *Nahrung*, vol. 30, no. 6, pp. 601–613, 1986.

[51] Y. Fang, L. Li, C. Inoue, L. Lundin, and I. Appelqvist, "Associative and Segregative Phase Separations of Gelatin/κ-Carrageenan Aqueous Mixtures," *Langmuir*, vol. 22, no. 23, pp. 9532–9537, Nov. 2006.

[52] L. M. Dimitrova *et al.*, "Limited coalescence and Ostwald ripening in emulsions stabilized by hydrophobin HFBII and milk proteins," *Colloids Surfaces A Physicochem. Eng. Asp.*, vol. 509, pp. 521–538, Nov. 2016.

[53] C. Huang, M. Moosmann, J. Jin, T. Heiler, S. Walheim, and T. Schimmel, “Polymer blend lithography: A versatile method to fabricate nanopatterned self-assembled monolayers,” *Beilstein J. Nanotechnol.*, vol. 3, pp. 620–628, Sep. 2012.

[54] M. Sprenger, S. Walheim, A. Budkowski, and U. Steiner, “Hierarchic Structure Formation in Binary and Ternary Polymer Blends,” *Interface Sci.*, vol. 11, no. 2, pp. 225–235, 2003.

[55] L. Cui, H. Wang, Y. Ding, and Y. Han, “Tunable ordered droplets induced by convection in phase-separating P2VP/PS blend film,” *Polymer (Guildf).*, vol. 45, no. 24, pp. 8139–8146, Nov. 2004.

[56] L. Xue, J. Zhang, and Y. Han, “Phase separation induced ordered patterns in thin polymer blend films,” *Prog. Polym. Sci.*, vol. 37, no. 4, pp. 564–594, Apr. 2012.

[57] C. Huang, A. Förste, S. Walheim, and T. Schimmel, “Polymer blend lithography for metal films: large-area patterning with over 1 billion holes/inch 2,” *Beilstein J. Nanotechnol.*, vol. 6, pp. 1205–1211, May 2015.

[58] G. Filippone, P. A. Netti, and D. Acierno, “Microstructural evolutions of LDPE/PA6 blends by rheological and rheo-optical analyses: Influence of flow and compatibilizer on break-up and coalescence processes,” *Polymer (Guildf).*, vol. 48, no. 2, pp. 564–573, 2007.

[59] J. Jůza and I. Fortelný, “Flow-Induced Coalescence: Evaluation of Some Approximations,” *Macromol. Symp.*, vol. 373, no. 1, pp. 1–10, Jun. 2017.

[60] I. Fortelný, J. Jůza, and B. Dimzoski, “Coalescence in quiescent polymer blends with a high content of the dispersed phase,” *Eur. Polym. J.*, vol. 48, no. 7, pp. 1230–1240, Jul. 2012.

[61] S. Roy and A. Sharma, “Self-organized morphological evolution and dewetting in

760 solvent vapor annealing of spin coated polymer blend nanostructures," *J. Colloid*
761 *Interface Sci.*, vol. 449, pp. 215–225, Jul. 2015.
762 [62] K. Ji-Seon, P. K. H. Ho, C. E. Murphy, and R. H. Friend, "Phase Separation in
763 Polyfluorene-Based Conjugated Polymer Blends: Lateral and Vertical Analysis of Blend
764 Spin-Cast Thin Films," *Macromolecules*, vol. 37, no. 8, pp. 2861–2871, 2004.
765 [63] T. Ghoshal *et al.*, "Size and space controlled hexagonal arrays of superparamagnetic
766 iron oxide nanodots: magnetic studies and application," *Sci. Rep.*, vol. 3, no. 1, p. Article
767 No. 2772, Dec. 2013.
768 [64] E. Guibal, T. Vincent, and R. Navarro, "Metal ion biosorption on chitosan for the
769 synthesis of advanced materials," *J. Mater. Sci.*, vol. 49, no. 16, pp. 5505–5518, Aug.
770 2014.
771 [65] V. Mohanasrinivasan *et al.*, "Studies on heavy metal removal efficiency and
772 antibacterial activity of chitosan prepared from shrimp shell waste.," *3 Biotech*, vol. 4,
773 no. 2, pp. 167–175, Apr. 2014.
774 [66] A. . Varma, S. . Deshpande, and J. . Kennedy, "Metal complexation by chitosan and its
775 derivatives: a review," *Carbohydr. Polym.*, vol. 55, no. 1, pp. 77–93, Jan. 2004.
776 [67] E. Guibal, "Interactions of metal ions with chitosan-based sorbents: a review," *Sep.*
777 *Purif. Technol.*, vol. 38, no. 1, pp. 43–74, Jul. 2004.
778 [68] N. Horzum, E. Boyacı, A. E. Eroğlu, T. Shahwan, and M. M. Demir, "Sorption
779 Efficiency of Chitosan Nanofibers toward Metal Ions at Low Concentrations,"
780 *Biomacromolecules*, vol. 11, no. 12, pp. 3301–3308, Dec. 2010.
781 [69] H. I. Okur *et al.*, "Beyond the Hofmeister Series: Ion-Specific Effects on Proteins and
782 Their Biological Functions," *J. Phys. Chem. B*, vol. 121, no. 9, pp. 1997–2014, Mar.
783 2017.

[70] M. K. Braun *et al.*, “Reentrant Phase Behavior in Protein Solutions Induced by Multivalent Salts: Strong Effect of Anions Cl – Versus NO 3 –,” *J. Phys. Chem. B*, vol. 122, no. 50, pp. 11978–11985, Dec. 2018.

[71] R. Senthil Kumar and P. Rajkumar, “Characterization of minerals in air dust particles in the state of Tamilnadu, India through FTIR, XRD and SEM analyses,” *Infrared Phys. Technol.*, vol. 67, pp. 30–41, Nov. 2014.

[72] T. F. Young, C. P. Chen, J. F. Liou, Y. L. Yang, and T. C. Chang, “Study on the Si–Si Vibrational States of the Near Surface Region of Porous Silicon,” *J. Porous Mater.*, vol. 7, no. 1/3, pp. 339–343, 2000.

[73] M. A. Girsova, G. F. Golovina, I. N. Anfimova, M. Y. Arsent’ev, and T. V Antropova, “Structure and spectral properties of the silver-containing high-silica glasses,” *J. Phys. Conf. Ser.*, vol. 741, no. 1, pp. 1–5, Aug. 2016.

[74] P. Garidel and H. Schott, “Fourier-Transform Midinfrared Spectroscopy for Analysis and Screening of Liquid Protein Formulations, Part 1,” *BioProcess Tech.*, vol. 4, no. 5, pp. 40–46, 2006.

[75] J. R. Smith, M. T. Cicerone, and C. W. Meuse, “Tertiary Structure Changes in Albumin upon Surface Adsorption Observed via Fourier Transform Infrared Spectroscopy,” *Langmuir*, vol. 25, no. 8, pp. 4571–4578, Apr. 2009.

[76] P. Murugaraj, D. E. Mainwaring, D. C. Tonkin, and M. Al Kobaisi, “Probing the dynamics of water in chitosan polymer films by dielectric spectroscopy,” *J. Appl. Polym. Sci.*, vol. 120, no. 3, pp. 1307–1315, May 2011.

[77] L. Guo, G. Liu, R.-Y. Hong, and H.-Z. Li, “Preparation and Characterization of Chitosan Poly(acrylic acid) Magnetic Microspheres,” *Mar. Drugs*, vol. 8, no. 7, pp. 2212–2222, Jul. 2010.

[78] P. Monvisade and P. Siriphannon, “Chitosan intercalated montmorillonite: Preparation, characterization and cationic dye adsorption,” *Appl. Clay Sci.*, vol. 42, no. 3–4, pp. 427–431, Jan. 2009.

[79] M. M. A. Al-Remawi, “Properties of Chitosan Nanoparticles Formed Using Sulfate Anions as Crosslinking Bridges,” *Am. J. Appl. Sci.*, vol. 9, no. 7, pp. 1091–1100, 2012.

[80] S. Kunjachan, S. Gupta, A. K. Dwivedi, A. Dube, and M. K. Chourasia, “Chitosan-based macrophage-mediated drug targeting for the treatment of experimental visceral leishmaniasis,” *J. Microencapsul.*, vol. 28, no. 4, pp. 301–310, Jun. 2011.

[81] T.-C. Yang and K. C. Saraswat, “Effect of Physical Stress on the Degradation of Thin SiO2 Films Under Electrical Stress,” *IEEE Trans. Electron Devices*, vol. 47, no. 4, pp. 746–755, 2000.

[82] F. Matteini, G. Tütüncüoğlu, D. Rüffer, E. Alarcón-Lladó, and A. Fontcuberta i Morral, “Ga-assisted growth of GaAs nanowires on silicon, comparison of surface SiOx of different nature,” *J. Cryst. Growth*, vol. 404, pp. 246–255, Oct. 2014.

[83] T. Ghoshal *et al.*, “Fabrication of ultra-dense sub-10 nm in-plane Si nanowire arrays by using a novel block copolymer method: optical properties.,” *Nanoscale*, vol. 8, no. 4, pp. 2177–87, Jan. 2016.

[84] R. Prakash, R. J. Choudhary, L. S. S. Chandra, N. Lakshmi, and D. M. Phase, “Electrical and magnetic transport properties of Fe3O4 thin films on GaAs (100) substrate,” *J. Phys. Condens. Matter*, vol. 19, no. 48, p. 486212, Dec. 2009.

[85] C.-Y. Shih *et al.*, “Two mechanisms of nanoparticle generation in picosecond laser ablation in liquids: the origin of the bimodal size distribution,” *Nanoscale*, vol. 10, no. 15, pp. 6900–6910, Apr. 2018.

[86] I. Prieto *et al.*, “Bi-modal nanoheteroepitaxy of GaAs on Si by metal organic vapor phase

epitaxy," *Nanotechnology*, vol. 28, no. 13, p. 135701, Mar. 2017.

[87] T. T. Morgan, T. M. Goff, and J. H. Adair, "The colloidal stability of fluorescent calcium phosphosilicate nanoparticles: the effects of evaporation and redispersion on particle size distribution," *Nanoscale*, vol. 3, no. 5, pp. 2044–2053, May 2011.

[88] J. Wallecan, C. McCrae, S. J. J. Debon, J. Dong, and J. Mazoyer, "Emulsifying and stabilizing properties of functionalized orange pulp fibers," *Food Hydrocoll.*, vol. 47, pp. 115–123, May 2015.

[89] W. N. Ha, F. Shakibaie, B. Kahler, and L. J. Walsh, "Deconvolution of the particle size distribution of ProRoot MTA and MTA Angelus.," *Acta Biomater. Odontol. Scand.*, vol. 2, no. 1, pp. 7–11, Jan. 2016.

[90] V. E. Ziegler and B. A. Wolf, "Bimodal drop size distributions during the early stages of shear induced coalescence," *Polymer (Guildf).*, vol. 46, no. 22, pp. 9265–9273, Oct. 2005.

[91] A. Rezaei Kolahchi, P. J. Carreau, and A. Ajji, "Surface Roughening of PET Films through Blend Phase Coarsening," *ACS Appl. Mater. Interfaces*, vol. 6, no. 9, pp. 6415–6424, May 2014.

[92] A. B. Reddy, G. S. M. Reddy, V. Sivanjineyulu, J. Jayaramudu, K. Varaprasad, and E. R. Sadiku, *Design and Applications of Nanostructured Polymer Blends and Nanocomposite Systems*, 1st ed. Elsevier Inc., 2016.

[93] F. Jara, O. E. Pérez, and A. M. R. Pilosof, "Impact of phase separation of whey proteins/hydroxypropylmethylcellulose mixtures on gelation dynamics and gels properties," *Food Hydrocoll.*, vol. 24, no. 6–7, pp. 641–651, Aug. 2010.

[94] N. Kimura, K. Kawazoe, H. Nakanishi, T. Norisuye, and Q. Tran-Cong-Miyata, "Influences of wetting and shrinkage on the phase separation process of polymer

mixtures induced by photopolymerization," *Soft Matter*, vol. 9, no. 35, p. 8428, 2013.

[95] T. Geldhauser, S. Walheim, T. Schimmel, P. Leiderer, and J. Boneberg, "Influence of the relative humidity on the demixing of polymer blends on prepatterned substrates," *Macromolecules*, vol. 43, no. 2, pp. 1124–1128, Jan. 2010.

[96] H. Zhang and F. Wang, "Analysis of surface wettability of synthetic magnetite," *J. Wuhan Univ. Technol. Mater. Sci. Ed.*, vol. 29, no. 4, pp. 679–683, 2014.

Graphical Abstract

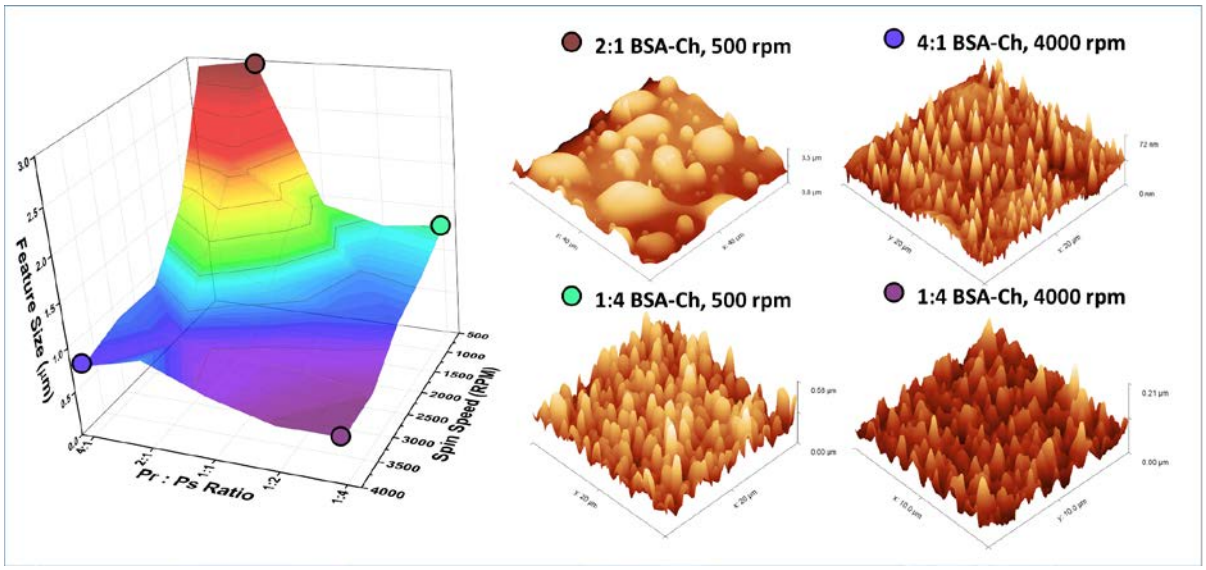

Supporting Information

Solution Preparation

Prior to dissolution, proteins, and polysaccharides were dried overnight at room temperature under vacuum. Biopolymer stock solutions were made by solubilising Ch and BSA in 90 % FA at 5 w/v%, 10 w/v%. These solutions were stirred in a closed vessel for 3 h at room temperature. The solutions were then centrifuged at 13,000 rpm in a Beckman Coulter Avanti J-26XPI centrifuge at 18 ºC for 15 min and decanted. Following this, stock solutions were stored at -20 ºC for further use or used immediately. Stock solutions were diluted with fresh FA and/or mixed with each other to produce coating solutions.

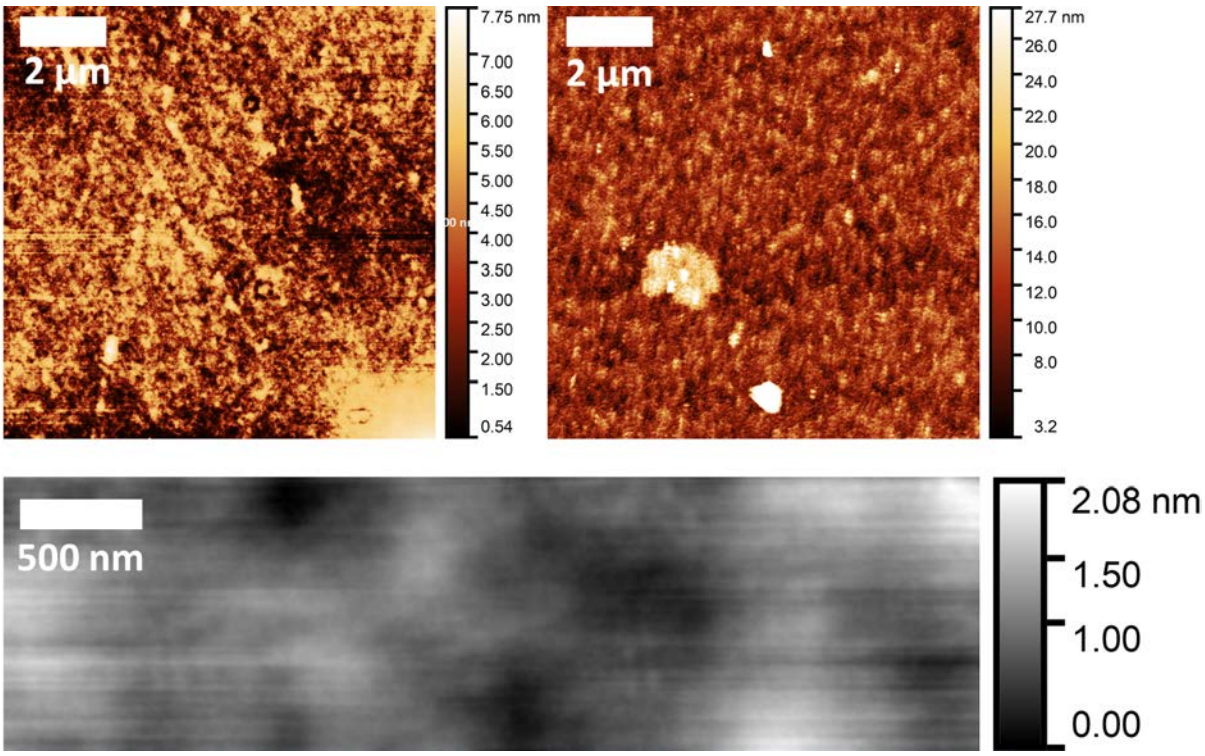

Figure S1: *AFM images showing results of casting neat thin-films at 65 % relative humidity at 2000 rpm prepared in the same manner as BSA-Ch blends. Biopolymer AFM images are red, glass substrate AFM image is grey. Shows 1% BSA film (left), 1% chitosan film (right) and glass substrate (bottom).* ***Scale bars top left hand corner of each image.***

885

886

887

888

889

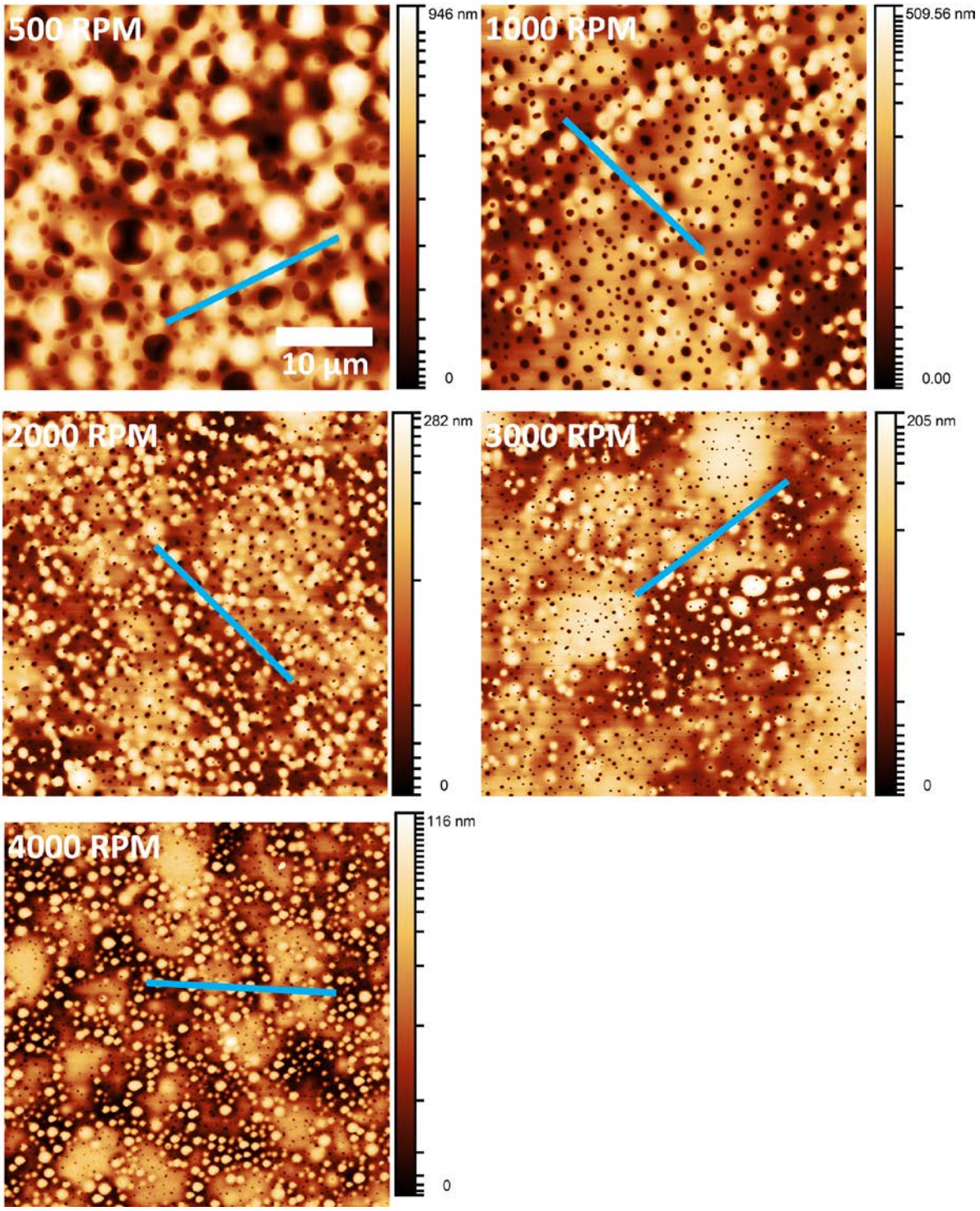

Figure S2: *AFM images depicting the effect spin speed in ambient air (65 % RH) for the 4:1 BSA-Ch blend. Each image is 40 µm × 40 µm area (scale bar 10 µm, shown in the 500 rpm image). Line profile denoted by blue line.*

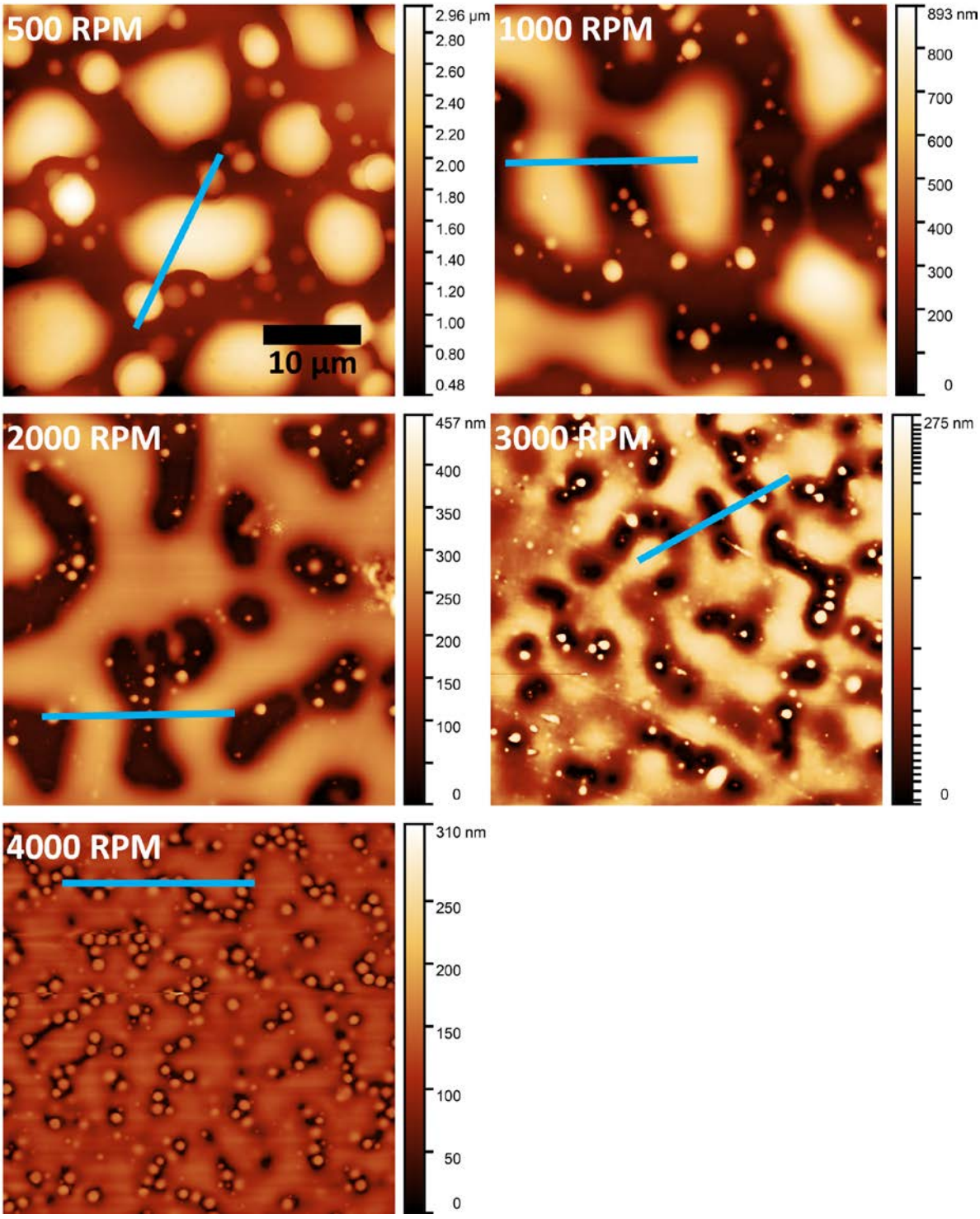

Figure S3: *AFM images depicting the effect spin speed in ambient air (65 % RH) for the 4:1 BSA-Ch blend. Each image is 40 µm × 40 µm area (scale bar 10 µm, shown in the 500 rpm image). Line profile denoted by blue line.*

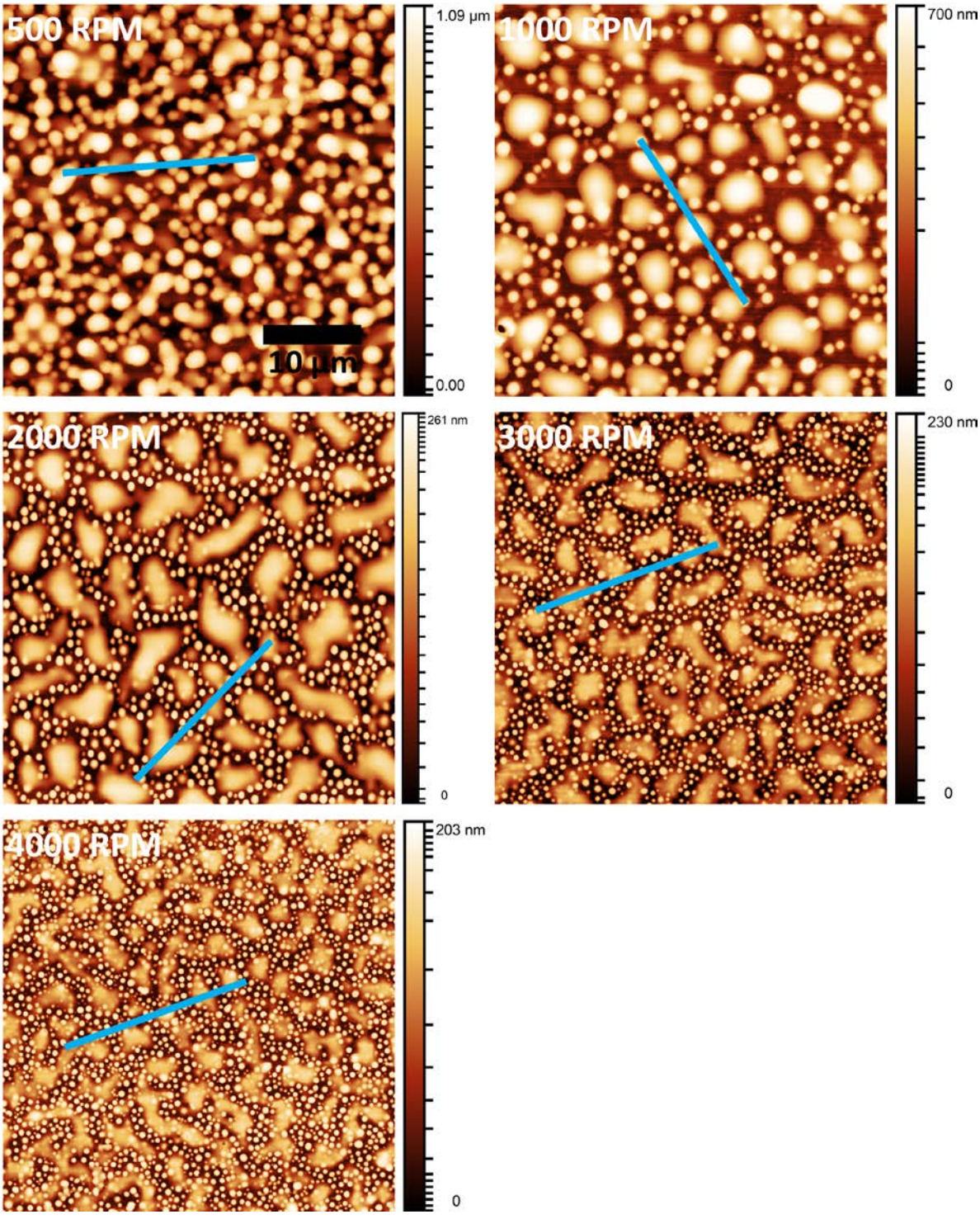

900

901 ***Figure S4:*** *AFM images depicting the effect spin speed in ambient air (65 % RH) for the*

902 *1:1 BSA-Ch blend. Each image is 40 µm × 40 µm area (scale bar 10 µm, shown in the 500*

903 *rpm image). Line profile denoted by blue line.*

904

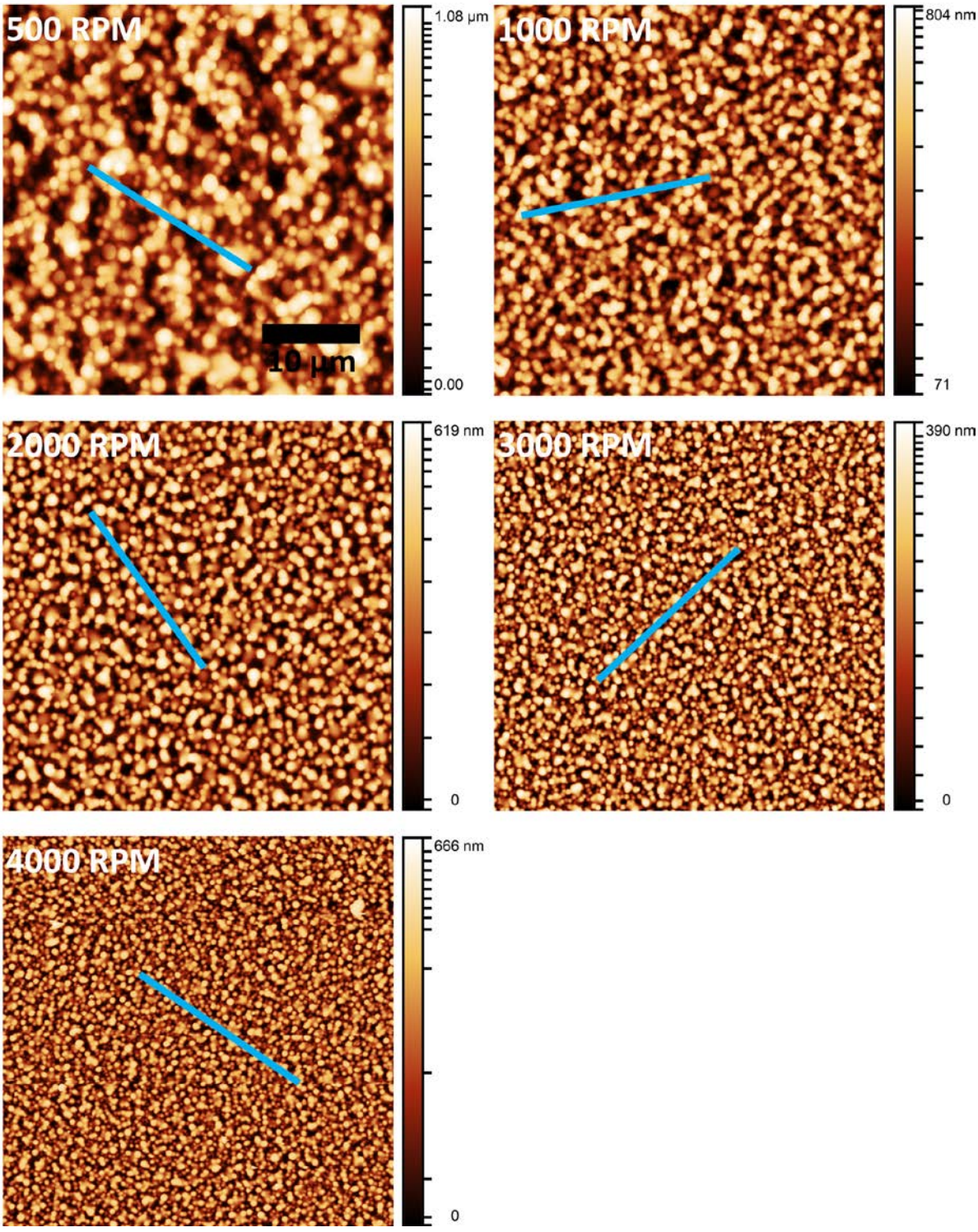

Figure S5: *AFM images depicting the effect spin speed in ambient air (65 % RH) for the 1:2 BSA-Ch blend. Each image is 40 µm × 40 µm area (scale bar 10 µm, shown in the 500 rpm image). Line profile denoted by blue line.*

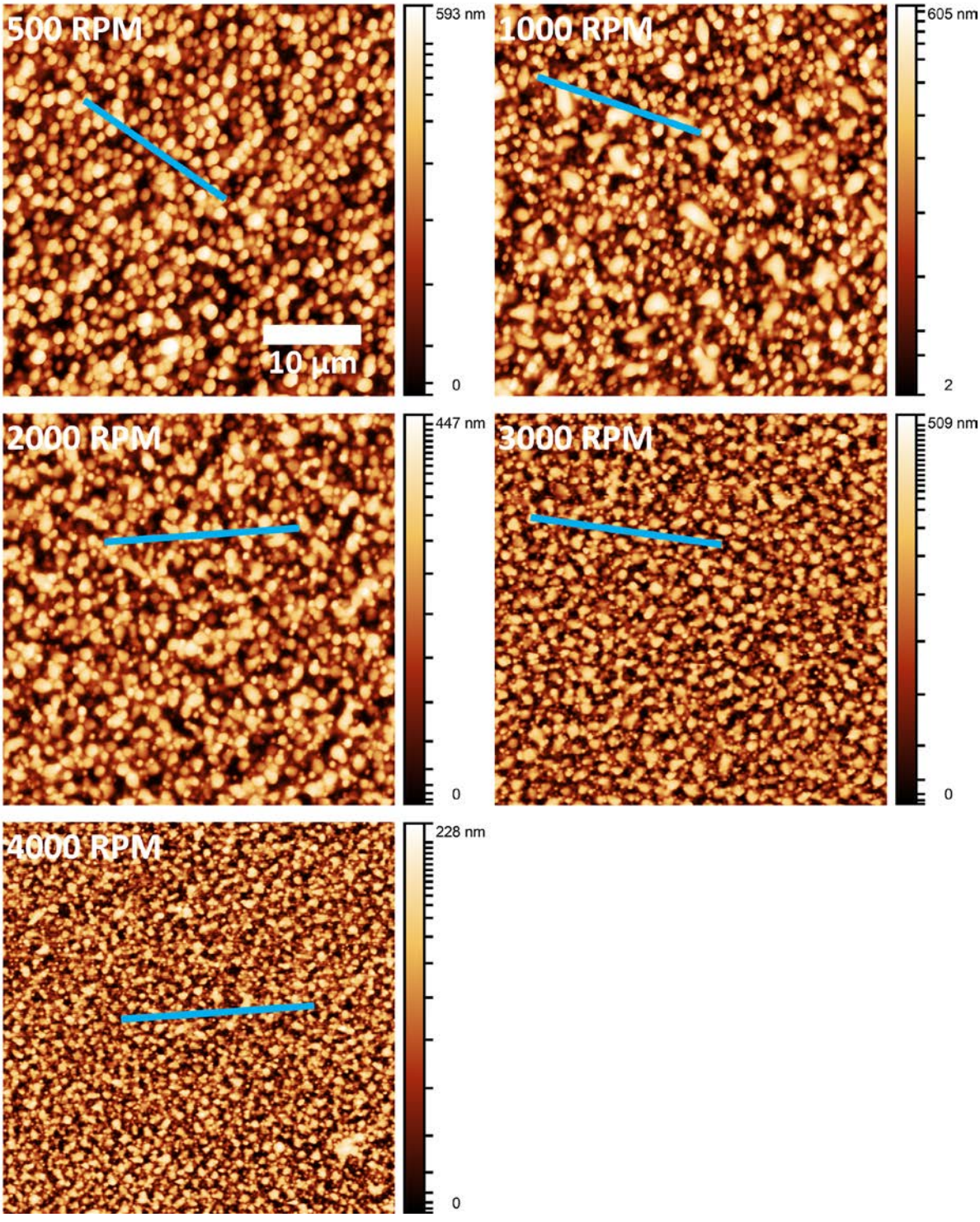

Figure S6: *AFM images depicting the effect spin speed in ambient air (65 % RH) for the 1:2 BSA-Ch blend. Each image is 40 µm × 40 µm area (scale bar 10 µm, shown in the 500 rpm image). Line profile denoted by blue line.*

914

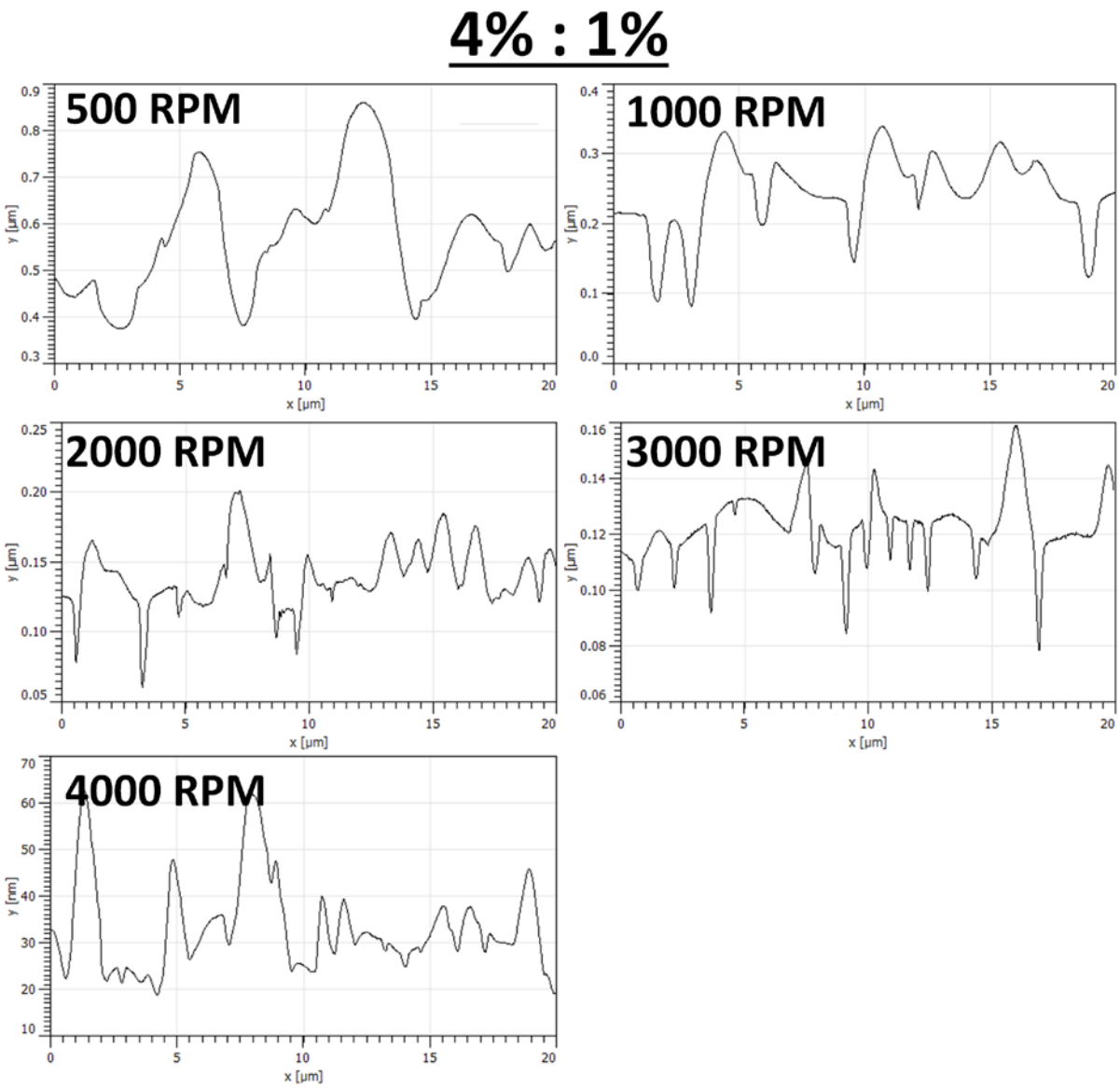

915

916 ***Figure S7:*** *20 µm line profiles for all 4:1 BSA-Ch.*

917

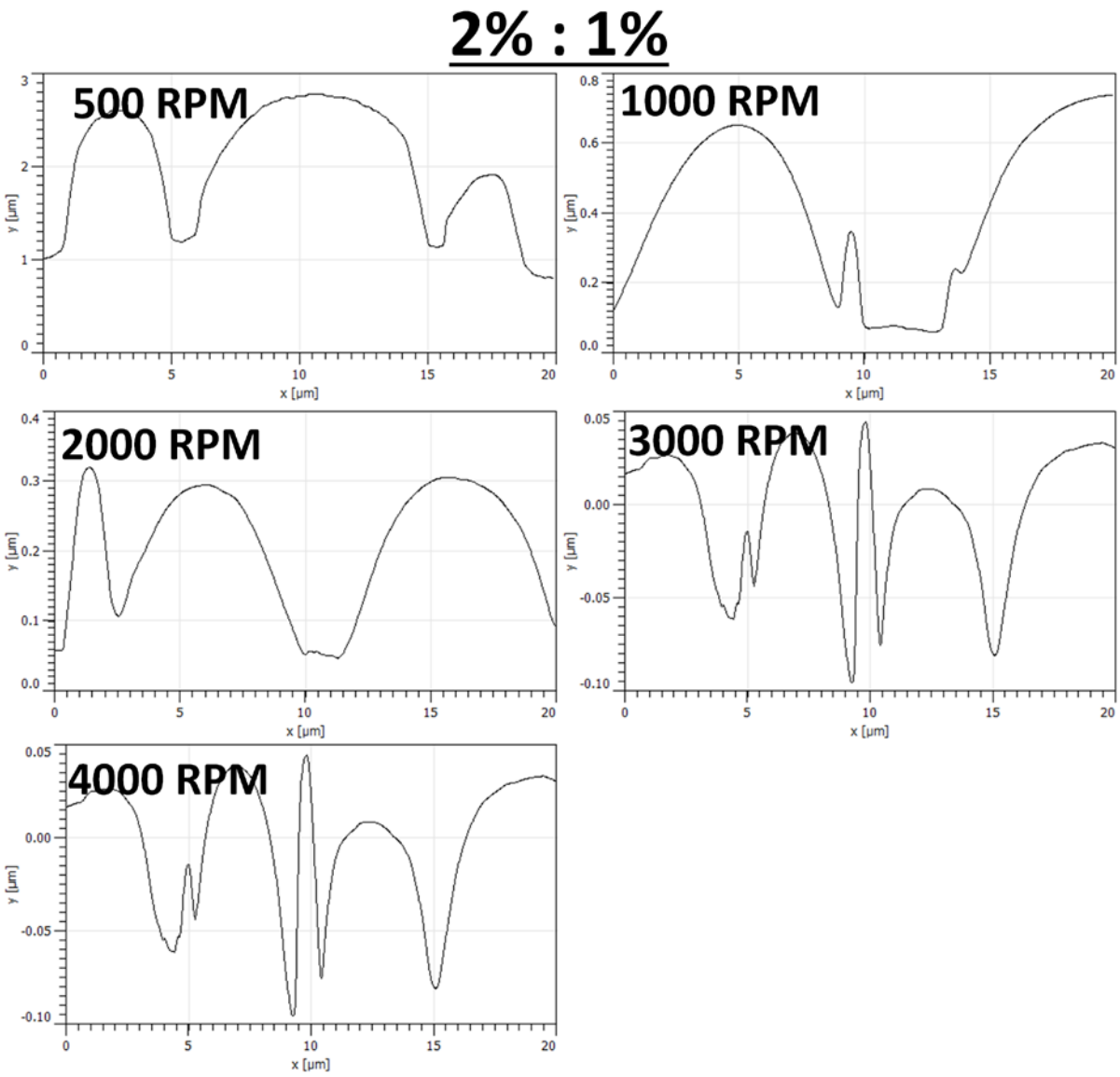

Figure S8: *20 µm line profiles for all 2:1 BSA-Ch.*

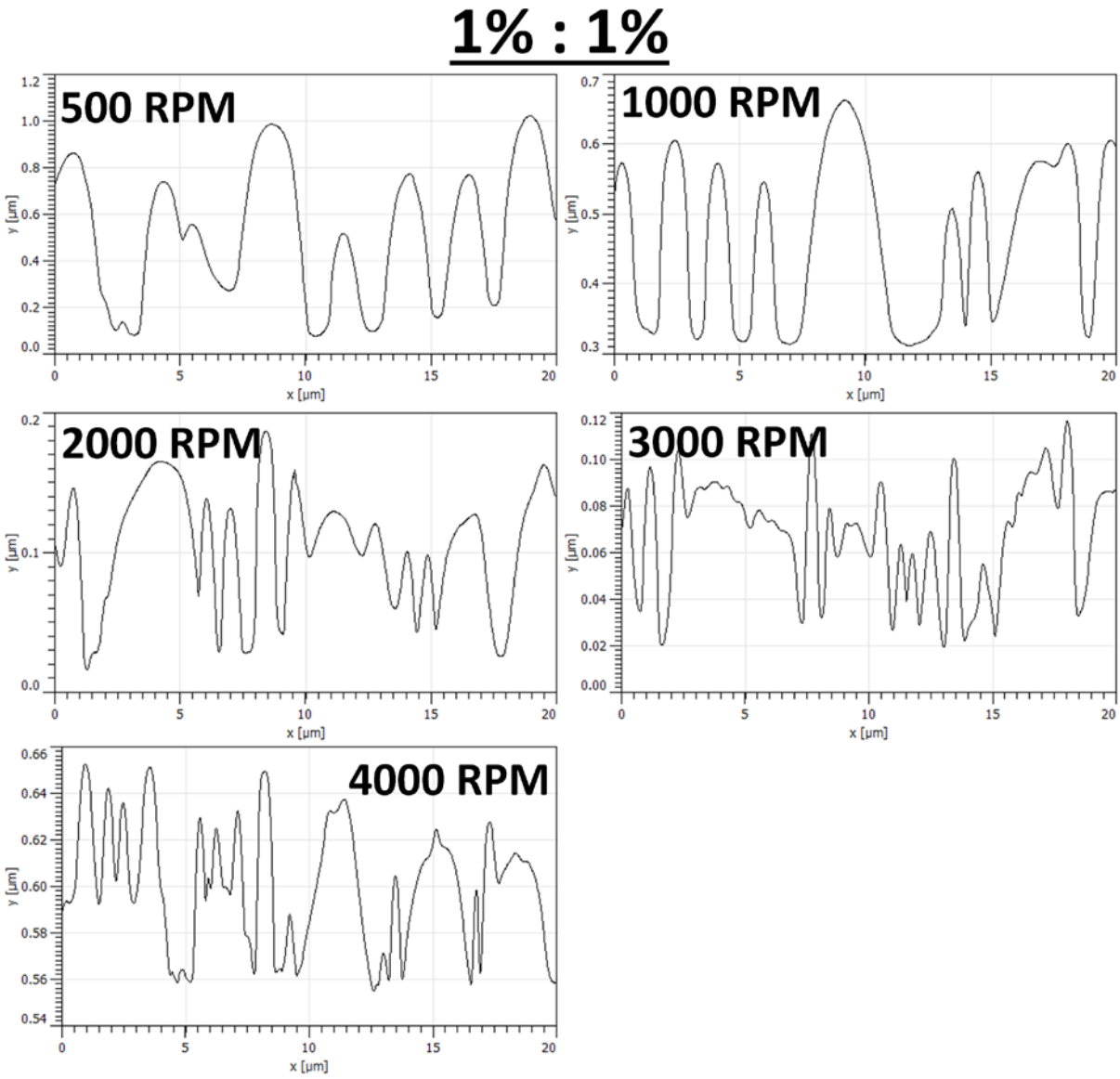

Figure S9: *20 µm line profiles for all 1:1 BSA-Ch.*

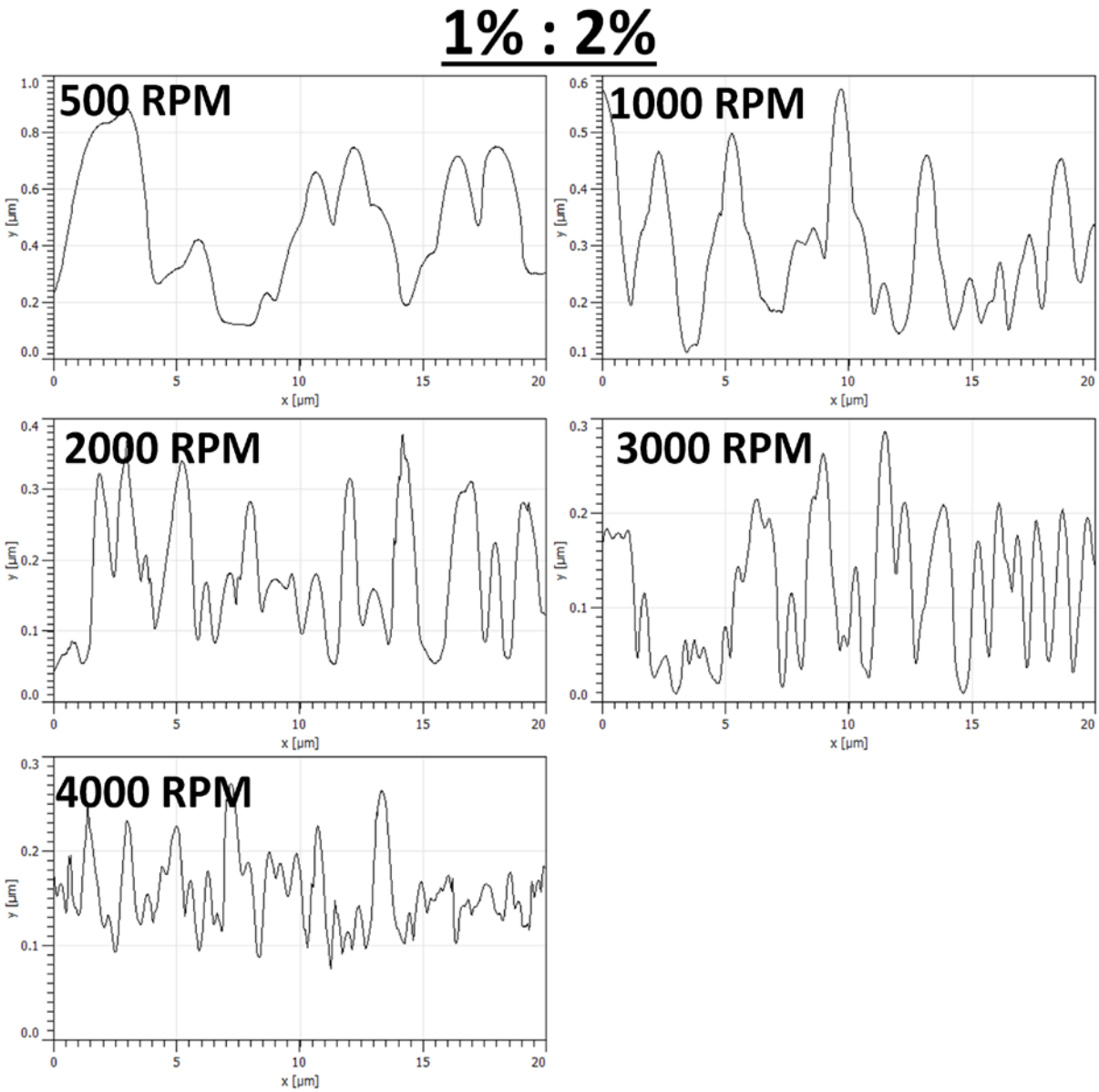

Figure S10: *20 µm line profiles for all 1:2 BSA-Ch.*

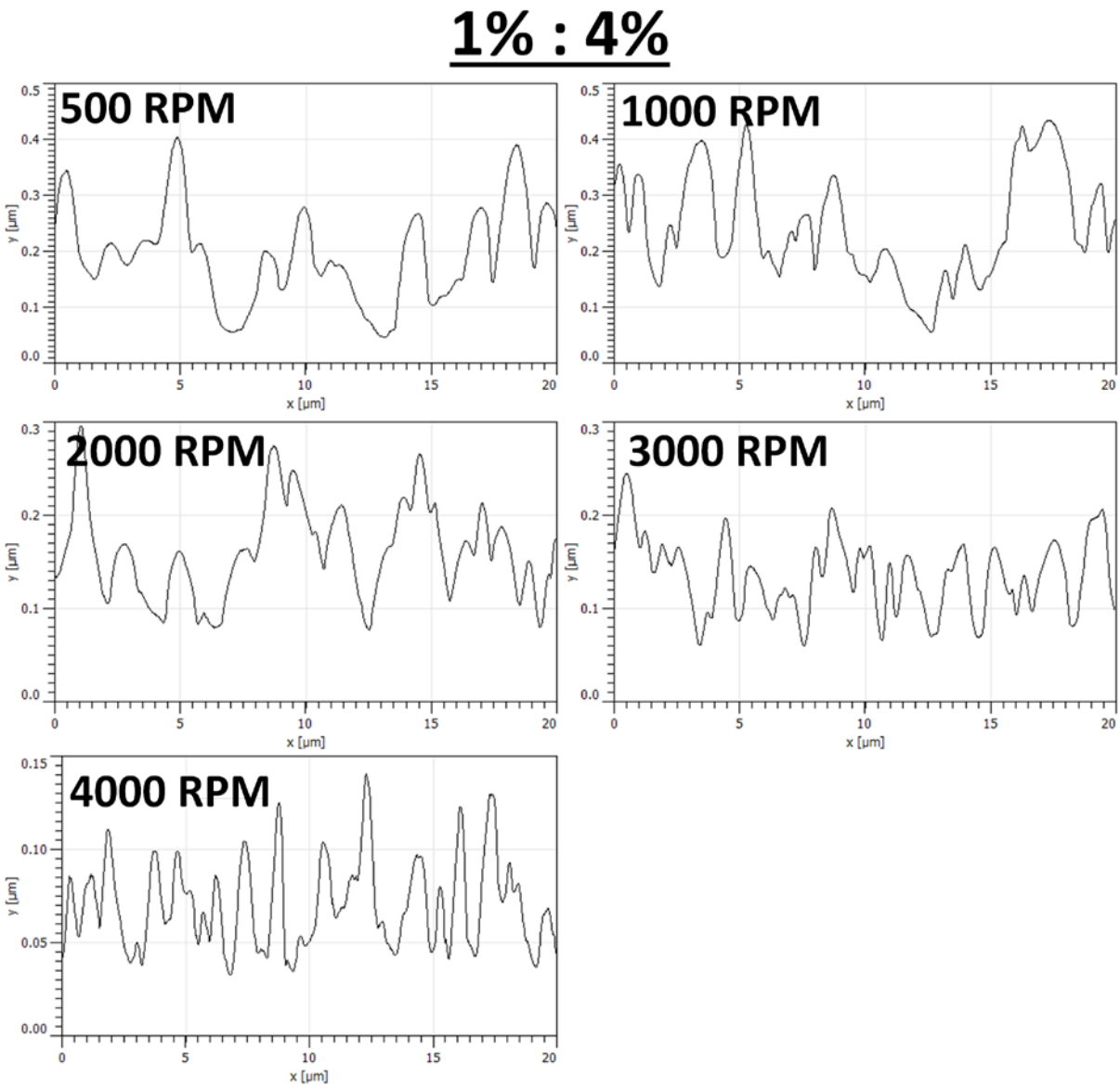

Figure S11: *20 µm line profiles for all 1:4 BSA-Ch.*

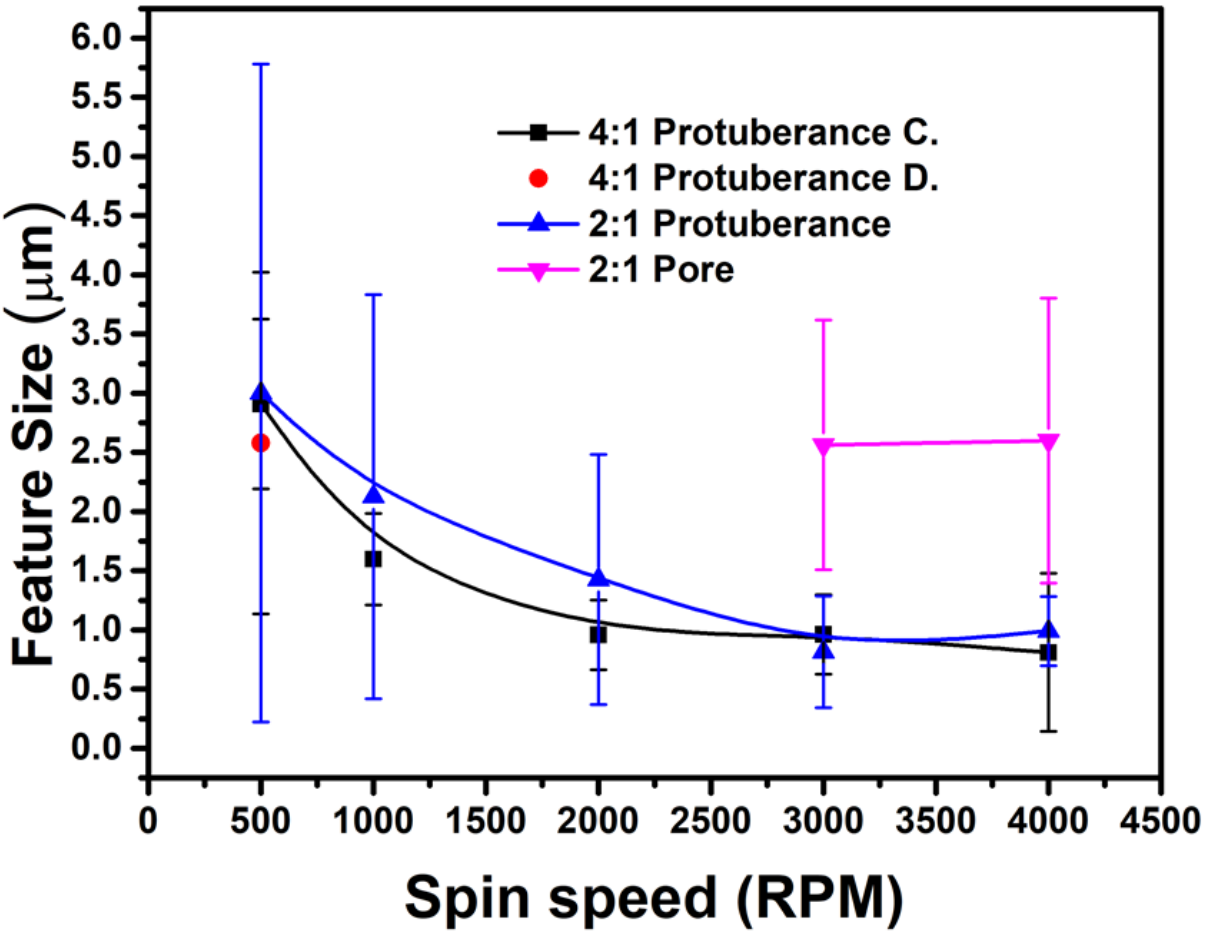

Figure S12: Statistical analysis of BSA-Ch blends feature diameter plotted against spin speed. All but the 2:1 blend refers to protuberance measurements, with the 2:1 blend data displaying both protuberance and pore data separately. The circular legend for the 4:1 blend refers to feature diameter in the discontinuous domain, i.e. salami structure regions.

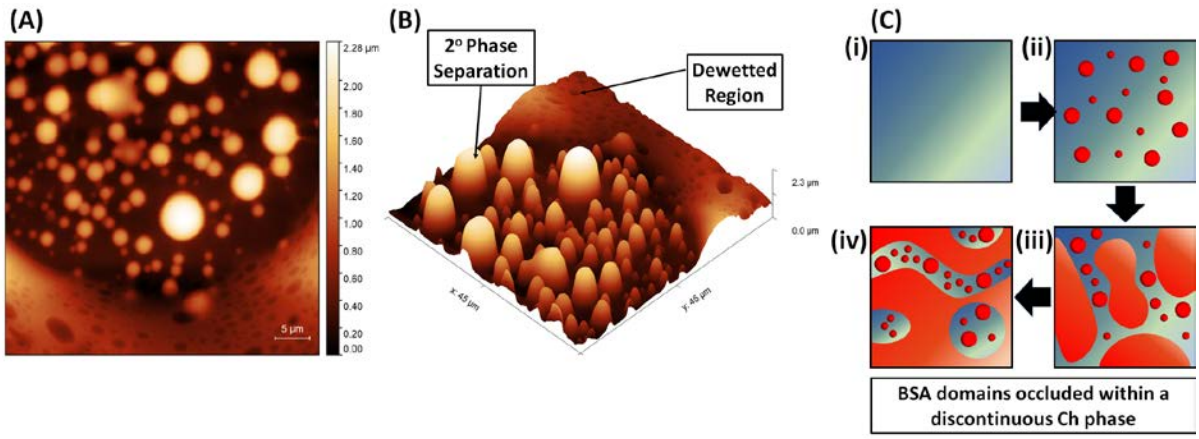

964

965 ***Figure S13: A*** *and* ***B)*** *2D and 3D AFM images of 4:1 BSA-Ch blend salami structures,*

966 *inset scale bar 5 µm.* ***C)*** *Mechanism of occlusion of the discontinuous phase.* ***Figure***

967 ***S7C (i)*** *shows homogenous solution before phase separation,* ***(ii)*** *shows blend phase*

968 *separation,* ***(iii)*** *shows elongated structures which may result from coalescence or high*

969 *shear forces and* ***(iv)*** *phase occlusion and adoption of salami structure.*

970

971

972

973

974

975

976

977

978

979

General Trends in Blend Thin-Film*s*

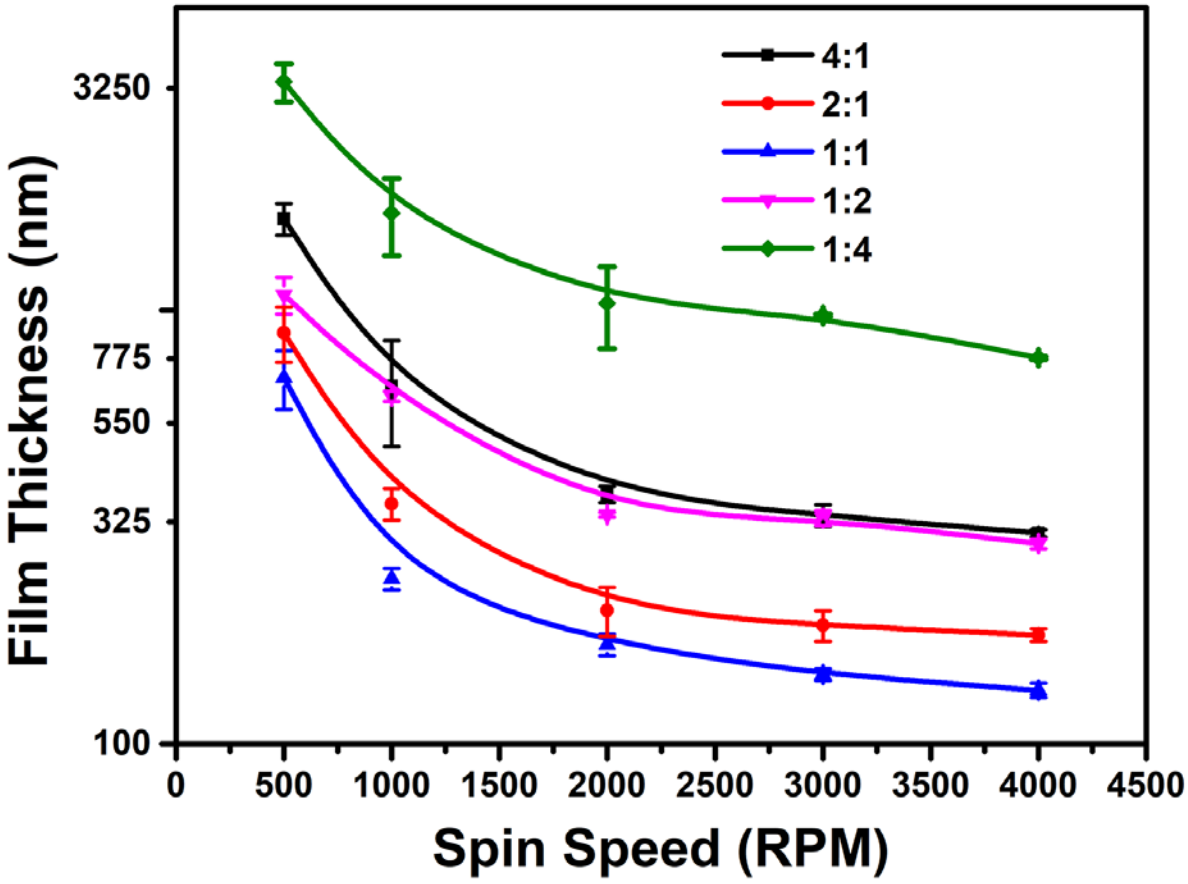

Figure S14: *Plots the average film thickness (nm) vs spin speed (rpm) for all BSA-Ch blends.*

Figure S14 **s**hows the average film thickness of BSA-Ch blends. 1:1 BSA-Ch films are the thinnest, due to low solution viscosity. Doubling the BSA wt % in the 2:1 BSA-Ch blends increases film thickness due to increased solution viscosity. As Ch produces more viscous solutions in formic acid, the 1:2 BSA-Ch blend produces thicker films than the 1:1 or 2:1 BSA-Ch blends. Similarly, the 4:1 BSA-Ch blend is thicker than the 2:1 BSA-Ch blend. However, at higher spin speeds (≥ 2000 rpm) 1:2 BSA-Ch blends have equivalent film thickness measurements to 4:1 BSA-Ch blends. This is most likely due to faster evaporation during spin

coating resulting in more viscous solutions. This, in turn, would result in more Ch retained on the substrate. As the most viscous solution, the 1:4 BSA-Ch films are the thickest. All blends (with the exception of the 1:4 BSA-Ch blend) achieved minimal reduction in film thickness with speeds exceeding 2000 rpm. The 4:1 BSA-Ch blend was the only blend to result in salami structure formation.

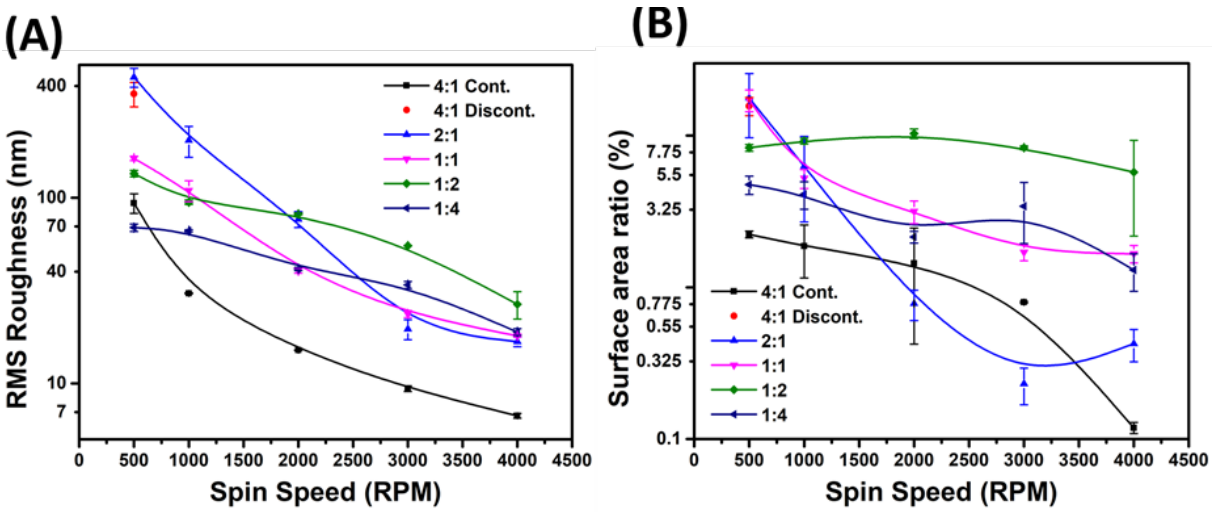

***Figure S15**: **A)** Plots the RMS roughness vs spin speed for all BSA-Ch blends. **B)** Plots the surface area ratio (%) vs spin speed for all BSA-Ch blends.*

Figure S15a shows the BSA-Ch blend film RMS roughness as a function of spin speed for all samples. RMS of polymer blends can affect coating properties such as hydrophobicity[23] and wettability[91] and bacterial adhesion.[31] Therefore, tailorable RMS is desirable. In all blends, roughness decreased with increased spin speed. Slopes of the 4:1 BSA-Ch blend were similar to the 2:1 blend, showing the sharpest reduction in RMS roughness from 500 rpm to 2000 rpm. For the 4:1 blend, this is likely due to a reduction in the diameter of all features as rpm increases. By contrast, the 2:1 blend loses large, tall features in favour of a smooth continuous BSA domain. At 4:1, 1:1, 1:2 and 1:4 ratios, protuberances become

oblate, pancake-like structures with increasing spin speed, thereby reducing RMS roughness. This also occurs in the 2:1 BSA blend, but to a lesser degree. Transitions in spin speed from 500 rpm to 1000 rpm reduced protuberance height from 4 μm to 600 nm resulting in the largest decrease in RMS roughness (242 nm, **Figure S15a**). However, a smooth continuous domain appears to be the predominant feature when determining RMS roughness for this blend.

Figure S15b plots surface area ratio (%) as a function of rotational speed in spin coating. In general, surface area ratio (%) is reduced with increased spin speed due to the reduced height of the structures. This result shows that aspect ratio of features can be tuned, allowing broader applicability. Higher aspect ratios are particularly useful for enhancing anti-reflective properties. This aligns with previous data seen with RMS roughness in **Figure S15a**. The 1:2 blend deviates from the general observation by increasing surface area ratio (%) with spin speed. This is due to interconnects (necks) forming between individual protuberances. As spin speed is increased from 500 rpm to 1000 rpm (**Figure 1**, D1 and D2), protuberance growth is inhibited by faster spin speed (**Figure 2a**). Protuberances however appear interconnected by a wall structure, referred to as a neck (i.e. inhibited coalescence).[58] As viscosity increases (due to increased concentration of the continuous phase) coalescence is supressed. This is to be expected as the adoption of a spheroidal shape is impeded.[40] These structures become more numerous as spin speed increases to 2000 rpm (**Figure 1**, D3) and growth is further inhibited. These interconnects increase the surface area ratio (%) of the sample. This is further supported by interconnects becoming less prominent at speeds exceeding 2000 rpm, though not totally removed (**Figure 1**, D4 and D5). In contrast to 4:1, 2:1 and 1:1 blends, the 1:2 blend features are compacted together and are not as well resolved from one another.

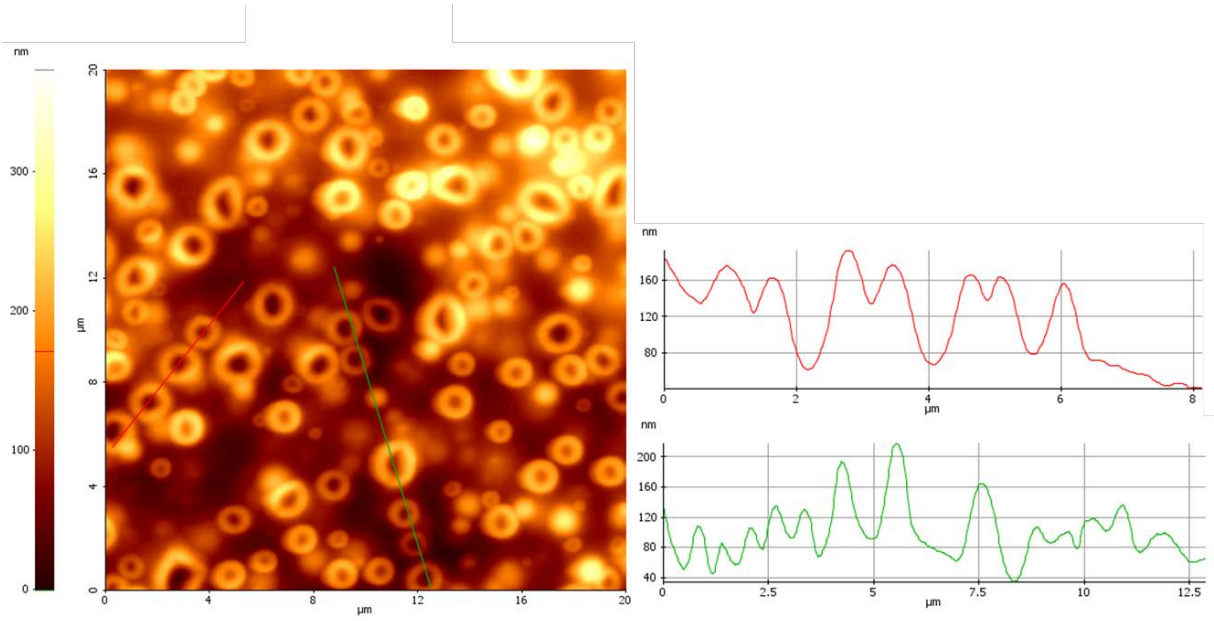

Figure S16: *AFM images and surface profiles of 1:4 BSA-Ch blends, 500 rpm on planar silicon substrates. Sample was etched using buffered solutions contained 200 mM Tris-HCl, pH 8.8 for 20 hrs after crosslinking with 20 wt% glutaraldehyde for 20 hr.*

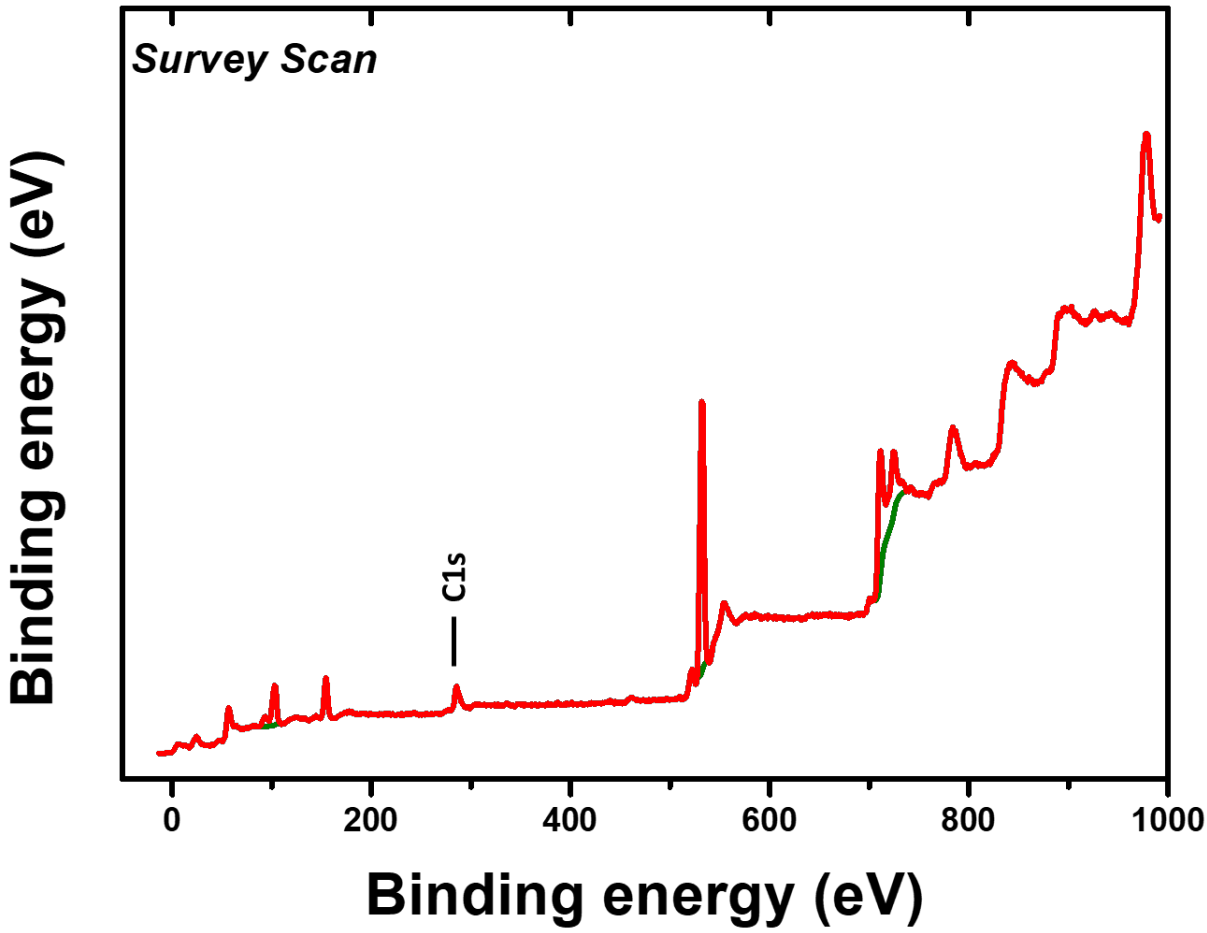

Figure S17: *Survey spectra of porous iron oxide matrix following calcination treatment.*

Pore Growth in Blend Thin-Films

At biopolymer ratio of 4 w/v% BSA to 1 w/v% Ch, across all spin speeds (**Figure 1**, Column A and **Figure S2**), pores (spherical holes) formed. Two relationships between pores and spin speed were observed: as spin speed increased, the mean pore diameter (**Figure 2a)** decreased and the number of pores per unit area (pores / μm^2, **Figure 2b**) increased. The mean pore diameter dropped from 1.14 μm (500 rpm) to 0.25 μm (4000 rpm), **Figure 2a**. Thus, pore formation at this biopolymer ratio occurs via an inhibited growth mechanism, *i.e.* a decrease in pore diameter with faster solvent removal.[23], [34], [40] The mechanisms of pore formation vary for each blend, unlike protuberances which show a consistent formation mechanism. The 2:1 BSA-Ch blend only forms “pseudo pores" (discontinuous indented regions caused by dewetting and phase inversion) at spin speeds ≥3000 rpm, unlike in the 4:1 blend. [15], [18], [19], [34], [92], [93] An increase in spin speed increased pore diameter and decreased the numbers of pores per area (**Figure 1**, Column B and **Figure S3**). This is in contrast to the trend observed with the 4:1 BSA-Ch blend which showed a decrease in pore diameter and an increase in pores per area with increased spin speed (**Figure 1**, Column A) which suggests a secondary phase inversion rather than salami structure formation.[17], [94]

Irregularly shaped pseudo pores are generated at ≥3000 rpm as phase inversion occurs (**Figure 1**, B3) due to the BSA component forming a continuous phase. Differences between the protein and polysaccharide phase viscosities at the 2:1 blend ratio, and strong shear forces at high spin speeds are the cause of phase inversion and phase elongation.[18][92] These shear stress effects also contribute to the increased pore diameter, the decreased number of features/area, and the irregular pore shapes.[18], [34] The pseudo pores observed in the 2:1 BSA-Ch blend are much larger than that of the pores caused by solvent-rich phase evaporation in the 4:1 blend (**Figure 1** Column A and B, **Figure 2A**). This is due to pseudo pores arising during the BSA continuous phase formation and shear effects in the 2:1 blend, whereas “true”

pores in the 4:1 blend appear to be formed from a solvent rich phase and solvent evaporation upon film vitrification.[53]

Figure 1, image B5 shows that 4000 rpm yields small, circular pores. The larger pores form longer continuous phases resulting in a minor increase of mean pore diameter. This indicates that the 2:1 BSA-Ch blend pore growth mechanism differs to that of the 4:1 blend, resulting from the formation of a continuous BSA phase.

Pore diameter data was also extracted from AFM images and the corresponding normalized frequency histograms are shown in **Figure S18**. The 4:1 BSA-Ch blend pores exhibited similar growth patterns to protuberances. At low spin speeds, the blends exhibit multimodal SDs over a broad diameter range. Increasing spin speed reduces the number of modes and population weight shifts to a smaller diameter (**Figure S18a**). This suggests that the pores, like the protuberances, develop via nucleation and growth. The 2:1 BSA-Ch blend produces a multimodal pore SD at high spin speeds (**Figure S18b**). These pores are irregularly shaped and do not form via the same process as 4:1 BSA-Ch blend pores (**Figure 1**, Column A).[26] They are caused by the BSA phase inverting and forming a continuous domain.[15] As such, increasing spin speed to 4000 rpm does little to shift the pore diameter, though the blend exhibits more pronounced peaks at 1.4 µm, 1.8 µm, 2.4 µm and 2.8 µm. It must be stated, however, that phase separation of polymer blends at high humidity and resulting pore formation is poorly understood.[26] Furthermore, humidity is not typically monitored, regulated or even discussed in the majority of polymer blend literature.[95] If pores are the desired morphological structure, removal of the discontinuous domain may be a more reliable manner of achieving a porous matrix.[57]

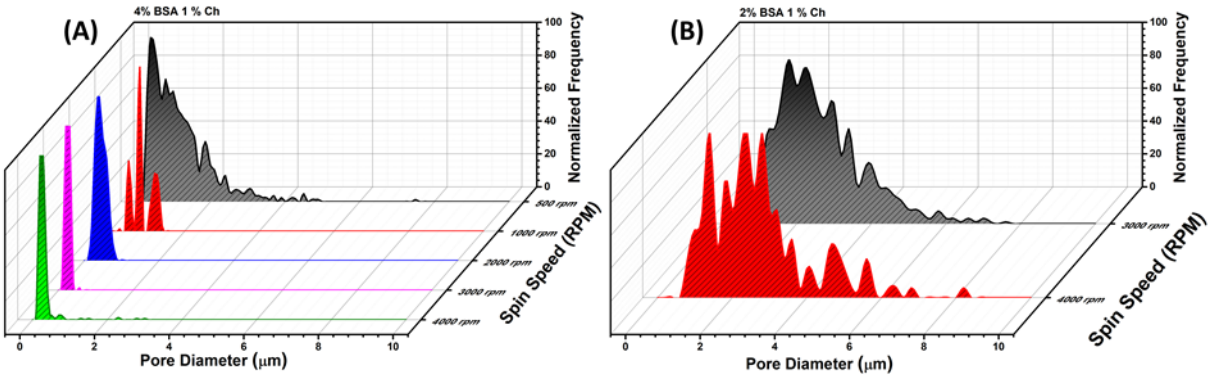

Figure S18: *Statistical analysis of BSA-Ch blends for feature diameter and frequency of feature diameters.* ***A)*** *Displays feature frequency vs diameter of observed features for the 4:1 blends and* ***B)*** *displays feature frequency vs diameter of observed features for the 2:1 blends respectively.*

Water Contact Angle

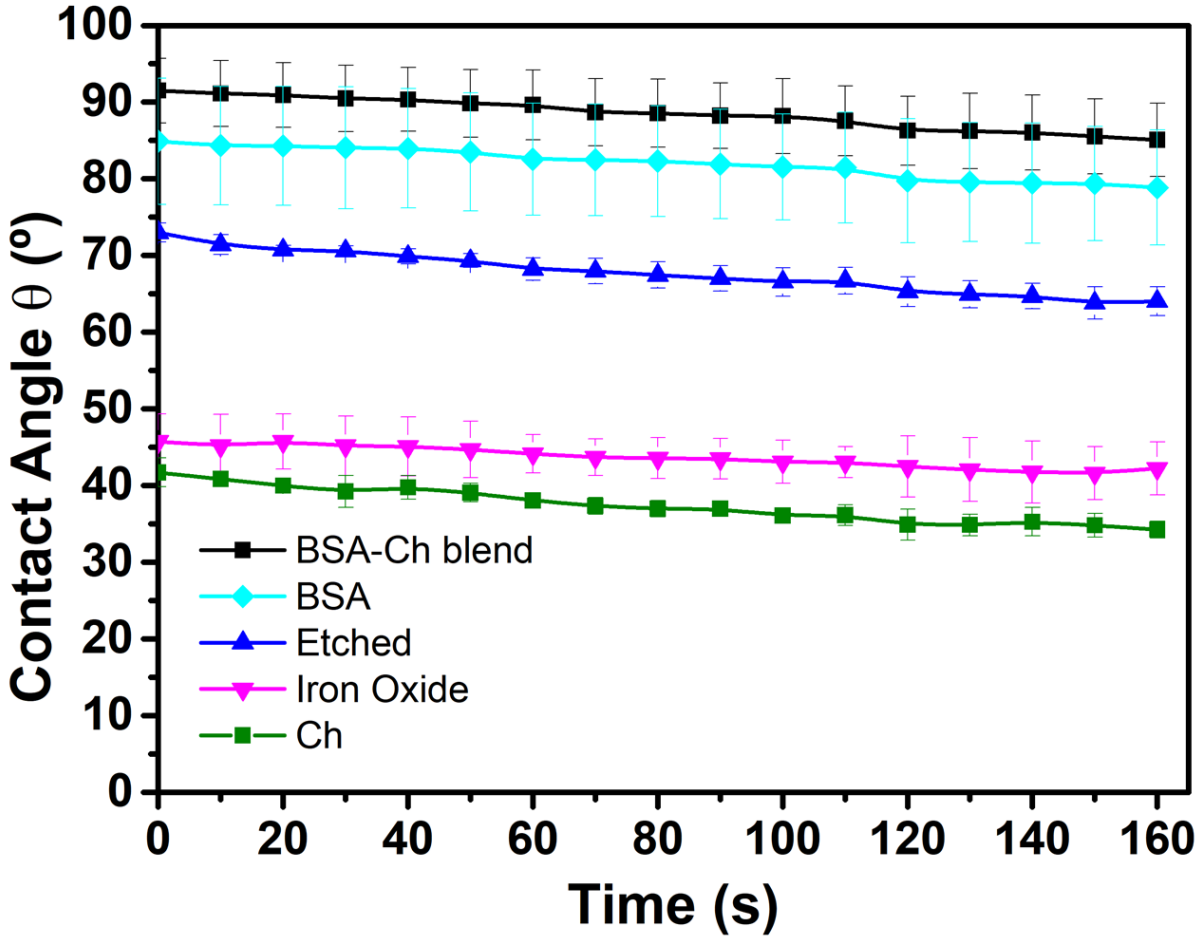

Figure S19: *Displays plot of average receding contact angle as a function of time for BSA, Ch, BSA-Ch blend, Tris-HCl etched blend and porous iron oxide matrix.*

Figure S19 shows water contact angles of the various relevant surfaces to confirm chemical and morphological changes in the samples with processing. This is to done to confirm the removal of BSA and the formation of a metal oxide on the surface to demonstrate correct assignment of each domain. All tested surfaces displayed a reduction in measured contact angle after 160 s. The 1:1 BSA-Ch blend exhibited the largest water contact angle, starting at 92º receding to 85º. This is unsurprising due to the rough nature of the blend surface and the incorporation of BSA, which is shown to have the second largest contact angle (85º – 79 º).[13] While on its own, water contact angle measurements do not confirm the removal of BSA or

formation of the metal oxide, these results compliment the findings of the etching, metal incorporation, FTIR and XPS.

The porous Ch matrix (73º – 64 º) has a higher contact angle than the pristine Ch surface (42º – 32 º): This is due to surface roughening caused by the pores. The reduction in the contact angle, compared to the 1:1 BSA–Ch, confirms the successful removal of BSA from the blend. Finally, the water contact angle of the iron oxide film (46º – 42 º) indicates magnetite composition, with the increased roughness and presence of pores contributing to a slightly larger contact angle than the literature.[96] The changes in the morphology and surface chemistry are as expected, and support the data seen in the FTIR and XPS spectra (**Figure 4**).